A&A 591, A5 (2016)
DOI: 10.1051/0004-6361/201527468

Astronomy & Astrophysics

ATLASGAL: A Galaxy-wide sample of dense filamentary structures⋆

Guang-Xing Li[1,2], James S. Urquhart[1,3], Silvia Leurini[1], Timea Csengeri[1], Friedrich Wyrowski[1], Karl M. Menten[1], and Frederic Schuller[4]

[1] Max-Planck-Institut für Radioastronomie, Auf dem Hügel 69, 53121 Bonn, Germany
e-mail: gxli@usm.lmu.de
[2] University Observatory Munich, Scheinerstr. 1, 81679 München, Germany
[3] Centre for Astrophysics and Planetary Science, University of Kent, Canterbury, CT2 7NH, USA
[4] European Southern Observatory, Alonso de Cordova 3107, Vitacura, Santiago, Chile

Received 29 September 2015 / Accepted 19 March 2016

ABSTRACT

Context. Filamentary structures are ubiquitous in the interstellar medium. Investigating their connection to the large-scale structure of the Galaxy and their role in star formation is leading to a paradigm shift in our understanding of star formation.
Aims. We study the properties of filamentary structures from the ATLASGAL survey, which is the largest and most sensitive systematic ground-based survey of the inner Galactic plane at submillimeter wavelengths.
Methods. We use the DisPerSE algorithm to identify spatially coherent structures located across the inner-Galaxy ($300^\circ < \ell < 60^\circ$ and $|b| < 1.5$). As a result we produce a catalogue of ~1800 structures; these were then independently classified by the five lead authors into one of the following types: marginally resolved, elongated structures, filaments, network of filaments and complexes. This resulted in the identification of 517 filamentary structures. We determine their physical properties and investigate their overall Galactic distribution.
Results. We find that almost 70% of the total 870 μm flux associated with these structures resides in filaments and networks of filaments and we estimate that they are likely to be associated with a similar fraction of the mass. Correlating these structures with tracers of massive star formation we also find that a similar fraction of the massive star forming clumps are associated with filaments and networks of filaments, which highlights the importance of these types of structures to star formation in the Galaxy. We have determined distances, masses and physical sizes for 241 of the filamentary structures. We find a median distance of 3.8 kpc, a mean mass of a few $10^3\,M_\odot$, a mean length of ~6 pc and a mass-to-length ratio of (M/L) ~200–2000 $M_\odot\,\mathrm{pc}^{-1}$. We also find that these filamentary structures are tightly correlated with the spiral arms in longitude and velocity, and that their semi-major axis is preferentially aligned parallel to the Galactic mid-plane and therefore with the direction of large-scale Galactic magnetic field. We find many examples where the dense filaments identified in ATLASGAL are associated with larger scale filamentary structures (~100 pc), and argue that this is likely to be common, and as such these may indicate a connection between large-scale Galactic dynamics and star formation.
Conclusions. We have produced a large and Galaxy-wide catalogue of dense filamentary structures that are representative of a particular size and mass range not previously well studied in the literature. Analyses of the properties and distribution of these filaments reveals that they are correlated with the spiral arms and make a significant contribution to star formation in the Galaxy. Massive star formation is ongoing within ~20% of the filaments and is strongly correlated with the filaments with the largest mass-to-length ratios. The luminosity of the embedded sources has a similar distribution to the Galactic-wide samples of young massive stars and can therefore be considered to be representative.

Key words. stars: formation – surveys – submillimeter: ISM – catalogs

1. Introduction

The presence of filamentary structures in interstellar clouds has been revealed by observations at different wavelengths and in different tracers over the last few decades (e.g. Schneider & Elmegreen 1979; Ungerechts & Thaddeus 1987). However, the importance of filaments in the process of star formation has only recently been fully realised thanks to the *Herschel* satellite. The high sensitivity, spatial dynamic range and angular resolution have revealed the ubiquity of filamentary structures throughout the interstellar medium (e.g., Molinari et al. 2010; André et al. 2010; Arzoumanian et al. 2011). Such filamentary structures have been found in both low- and high-mass star-forming molecular clouds, as well as in quiescent clouds (e.g. Miville-Deschênes et al. 2010). In nearby molecular clouds, a substantial fraction of pre-stellar cores are located on filaments, suggesting that the formation of filaments is a step preceding star formation (see André et al. 2014, and references therein).

The mechanisms leading to their formation and their link to the star formation process is not well understood. Filaments can form through compression or shear at a scale that is comparable to the filament length. This can be achieved with gravitational instabilities, gravitational collapse (e.g. Burkert & Hartmann 2004; Gómez & Vázquez-Semadeni 2014; Li et al. 2015), supersonic turbulence (Padoan et al. 2001; Heitsch et al. 2008), and converging flows (Heitsch et al. 2008; Vázquez-Semadeni et al. 2011). Turbulence can produce filaments through a combination of compression and shear (Hennebelle 2013; Federrath 2016; Moeckel & Burkert 2015; Arzoumanian et al. 2011). Their physical characteristics are constrained by a relatively limited

⋆ Full Tables 1 and 3 and the FITS files associated to Fig. 9 are only available at the CDS via anonymous ftp to cdsarc.u-strasbg.fr (130.79.128.5) or via http://cdsarc.u-strasbg.fr/viz-bin/qcat?J/A+A/591/A5

number of examples in the literature; filamentary structures have been reported showing a broad range of lengths, from a few parsecs (Schisano et al. 2014) to large-scale structures of several tens to hundreds of parsecs (e.g. Li et al. 2013; Goodman et al. 2014; Ragan et al. 2014; Wang et al. 2015) with a variety of aspect ratios, widths and masses.

To fully understand their origin, subsequent evolution, and thus their role in star formation, systematic studies of large samples of filamentary structures are necessary. Unbiased surveys of the inner Galactic plane, and of entire star-forming regions at submillimetre and far-infrared wavelengths are providing a rich database for such studies. Such surveys include the Hi-Gal (Molinari et al. 2010) and Gould Belt projects, (André et al. 2010) both of which cover the wavelength regime 70 μm–500 μm with *Herschel*, as well as the APEX Telescope Large Area Survey of the Galaxy (ATLASGAL) survey (Schuller et al. 2009).

In this paper we present the first systematic search for filamentary structures across the inner Galactic plane at submillimetre wavelengths based on the ATLASGAL survey. ATLASGAL covered 420 square degrees of the inner Galactic plane at 870 μm with an angular resolution of 19.2″. Emission from dust is optically thin at this wavelength and therefore ATLASGAL is an excellent tracer of column density and total mass (Schuller et al. 2009). In the ATLASGAL survey data, diffuse emission is filtered out, leaving only the compact high density structures. The ATLASGAL maps are not affected by saturation. These properties make the ATLASGAL emission maps an ideal place to conduct the first Galactic-wide search for filaments. Furthermore, having a wealth of ancillary data in hand from complementary ATLASGAL follow-up programmes (e.g., Wienen et al. 2012, 2015; Giannetti et al. 2014), we are able to assign distance estimates to the extracted structures, allowing a direct estimate of their physical properties.

The structure of the paper is as follows: in Sect. 2 we describe the procedures used to identify coherent structures from the dust emission maps and describe how their properties are determined. The classification scheme is described in Sect. 3 where we also discuss the differences in the structural and statistical properties of the various type of structures identified. We determine velocities, distances, masses, lengths and widths for the filamentary structures in Sect. 4. In Sect. 5 we investigate their connection to larger scale structures such as giant molecular filaments (e.g. Li et al. 2013; Ragan et al. 2014; Goodman et al. 2014) and the spiral arms. In this section we also investigate their association with infrared dark clouds, H II region bubbles and massive star formation in an effort to link these structures to other catalogues and evaluate their contributions to star formation in the Galaxy. In Sect. 6 we present a summary of this work and highlight our main findings.

2. Identifying structures

The ATLASGAL survey (Schuller et al. 2009) covers 300° < ℓ < 60° and $|b|$ < 1.5°. It has a typical noise level of 50–70 mJy beam^{-1} and is sensitive to gas with H_2 column densities exceeding ~10^{22} cm^{-2}. For our sample, the beam size of ATLASGAL (which is 19.2 arcsec) corresponds to ~0.4 pc at a typical distance of ~4 kpc. Submillimetre emission detected from the ground are dominated by fluctuations from the atmosphere. To remove these fluctuations, median values of the correlated emission between all bolometers are subtracted in the data reduction process. A consequence of this is that uniform emission on scales larger than ~2.5 arcmin are filtered out. However, structures larger than this can be recovered provided that the structures are compact enough (Schuller et al. 2009) and therefore filamentary structures will be preserved as long as their widths are smaller than the scale above which filtering is effective.

We aim to study filamentary structures in the ATLASGAL survey. This has been achieved through two steps. First, we extract skeleton representations of structures in the dust continuum emission maps with the Discrete Persistent Extractor (`DisPerSE`; Sousbie 2011). Then, the extracted structures are classified, and filamentary structures are identified. In this section we describe the extraction of structures. The classification of the extracted structures into different categories will be described in the following section.

2.1. Extraction of skeletons

We use the publicly-available `DisPerSE` (Discrete Persistent Extractor; Sousbie 2011)[1] source extraction algorithm to identify large spatially coherent structures that are located within the ATLASGAL survey region. This algorithm is based on discrete Morse theory and identifies persistent topological features such as peaks, voids, walls, and in particular, filamentary structures from 2D or 3D datasets. The resulting skeletons[2] extracted by `DisPerSE` are therefore representations of the topological structure of the emission. `DisPerSE` has been successfully used to trace structures in *Herschel* data (e.g. André et al. 2010; Hill et al. 2011; Arzoumanian et al. 2011) as well as on column density maps produced by simulations (e.g. Smith et al. 2014b). A number of other algorithms have been used in recent studies (e.g. *getfilaments* – Men'shchikov 2013, *CuteX* – Molinari et al. 2011 and Hessian matrix method – Schisano et al. 2014), however, with the except of *getfilaments*, none are currently publicly available. We therefore decided to use `DisPerSE`, as it is the most widely used code for this purpose in the literature and has been shown to produce reliable results (e.g. André et al. 2010; Hill et al. 2011; Arzoumanian et al. 2011).

The two most important parameters of the program are the persistence (p) and robustness (r) thresholds. The persistence threshold is a measure of the absolute difference of the values of a pair of critical points, while the robustness threshold is a measure of the contrast of a structure with respect to the local background. In order to determine the optimal values for these two thresholds we tried different combinations on a test field. The region selected for these tests was $\ell \sim 22.5°$ as it contains a large filamentary structure as well as a number of molecular complexes and was therefore considered an ideal region to test the code.

We applied the `DisPerSE` algorithm to ATLASGAL tiles with a pixel size of 6″. Initial tests on the ATLASGAL emission maps revealed two difficulties. First, the noise varied over the field and is significantly higher in the upper and lower thirds of the maps (i.e. $|b| > 1°$). `DisPerSE` only allows a single value for the thresholds and so results in large numbers of spurious structures being detected in these noisy regions. This problem can be significantly reduced using signal-to-noise ratio maps for the initial identification of structures. This technique has been successfully applied in our previous works (e.g. Csengeri et al. 2014). The second problem is related to the

[1] `http://www2.iap.fr/users/sousbie/web/html/indexd41d.html?`

[2] A skeleton is a set of connecting points that trace the high-density "crests" of the emission map.

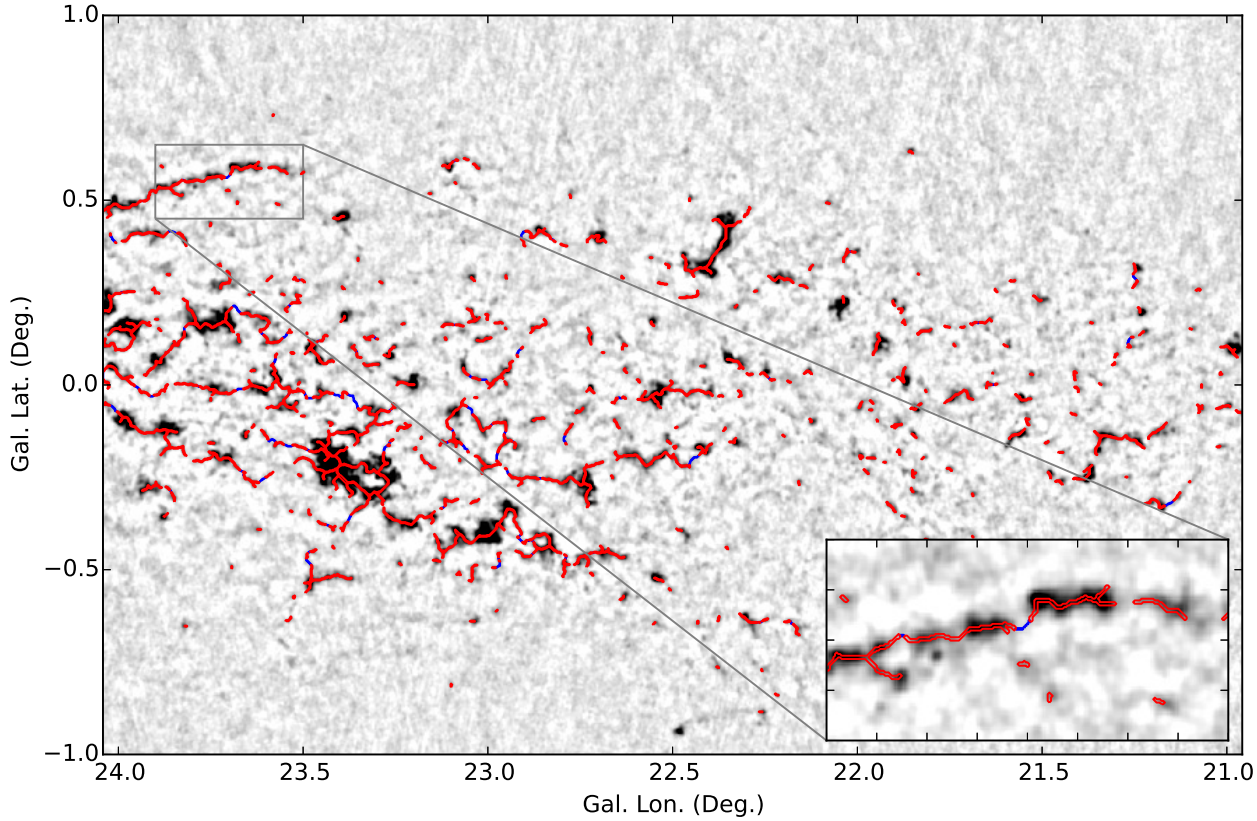

Fig. 1. Emission map of the $\ell = 22°$ field that has been used to optimise the persistence and robustness thresholds used by `DisPerSE`. This map is overlaid with the skeletons obtained using a high robustness threshold that trace the high-column density regions shown in red (i.e. $p = 1.4$ and $r = 2.5$) and the inter-connecting skeletons obtained using a lower robust threshold that traces the lower column density connecting regions are shown in blue (i.e. $p = 1.4$ and $r = 1.95$).

ground-based nature of the survey; in order to remove the contribution of the sky the median value of the correlated emission between all bolometers is removed. Although this is a very effective way of removing the sky noise, it also filters out coherent emission from large-scale structures. As a result, filamentary structures might appear as chains of disconnected fragments in the ATLASGAL emission maps, and `DisPerSE` does not identify them as a single structure. In order to increase the sensitivity of the survey for the diffuse emission, we smoothed the maps using a Gaussian kernel with a FWHM of twice the ATLASGAL beam. This lowers the overall resolution by a factor 2.2 (∼42″, which corresponds to a FWHM of ∼7 pixels in the maps) but significantly increases the sensitivity to the lower column density regions by roughly a factor of 4.

Our primary goal is to detect and quantify coherent dust condensations in the ATLASGAL survey, and as a result a good skeleton of the emission has to satisfy the following requirements: first, it should trace structures that appear to be coherent, and second, noise should not be represented by the skeleton. Investigating the performance of `DisPerSE` with different combinations of parameters we found that the skeleton from a single set of values for the persistence and robustness parameters was not sufficient to obtain a good representation of the emission seen in the maps. Either the parameters were too constraining and only the highest column density regions were picked up or they were too permissive, resulting in large numbers of spurious sources. We therefore settled for two sets of parameters and carefully filtered the results to identify a reliable sample of coherent structures.

The final skeleton used in the analysis is constructed as follows: first, we make a catalogue of short skeletons that trace the high-column density dust condensations using a high robustness parameter. This is used to make a primary catalogue of reliable fragments. We then try to connect these fragments to identify larger coherent structures using a lower robustness threshold, which is more sensitive to the lower column density regions between the dense clumps. The primary skeleton is produced with $p = 1.4$ and $r = 2.5$, in which only structures with significant contrast are included, and the secondary skeleton is produced with $p = 1.4$ and $r = 1.95$. We combined the results of these two extractions to produce a reliable catalogue for further analysis. In Fig. 1 we show the result of this two stage procedure for the test field. In this image the primary skeletons that trace the high-column density fragments are shown in red while the lower column density interconnecting fragments are shown in blue. The interconnecting fragments are only included in the analysis if (a) lengths of the segments are shorter than 4 pixels, or (b) average flux of the pixels on the skeleton is larger than 4 times the image rms.

We found that even with a relatively conservative threshold the output produced by `DisPerSE` still contained structures that have low signal-to-noise ratios. Therefore to ensure the reliability of the catalogue produced from our analysis we removed any structures that are approximately 4.5 times smaller than the smoothed beam (e.g. <30 pixels) in order to focus the catalogue on the filamentary structures; this has the consequence of excluding shorter and perhaps more distant structures.

A visual inspection of the maps confirms that the method described above is able to recover all of the most significant

structures that would be identified by eye and provides confidence that nothing important has been missed. Although we have developed our method to ensure that all important structures are recovered, our catalogue is limited by the sensitivity and resolution of the observations.

3. Classification

3.1. Classification scheme

Following the procedure presented in Sect. 2.1 we have produced a preliminary catalogue of 1812 structures. They cover a range of sizes, morphologies and complexity from relatively roundish featureless blobs to large star forming complexes. The emission associated with the more complicated regions is often blended and the underlying structure is unclear, making interpretation of any derived properties difficult.

Based on a visual inspection of the observed properties of the catalogue sources we were able to identify a relatively small number of common types of objects that can be used to broadly classify the whole sample. Below we provide a list of the six classes and a brief description of their observed properties:

1. Marginally resolved clumps: structures that appear as relatively isolated structures with simple morphologies and small aspect ratios (<2). We also use this classification for small groups of isolated clumps that have no obvious connecting emission.
2. Resolved elongated structures: structures classified in this group are dominated by elongated structures with aspect ratios of 2–3 and a relatively small number of associated spine points (<100 pixels). These may simply be unresolved filaments or fragments of larger filaments where the connecting lower density gas does not have sufficient column density to have been detected by ATLASGAL. This class also includes unresolved structures that are extended in more than two directions; these typically consist of one or two central bright clumps associated with three of four lower density strands protruding radially away from the centre.
3. Filaments: elongated linear structures that are clearly resolved across their lengths and widths and consisting of a single dominant filament with relatively few sub-branches and typical aspect ratios larger than 3.
4. Networks of filaments: several filaments that seem to be connected to each other. In many cases these networks are coincident with similar networks of infrared-dark clouds (IRDC) that are seen in absorption at mid-infrared wavelengths against bright Galactic background emission.
5. Complexes: they are regions of very bright extended and often complex emission, and although `DisPerSE` has connected the emission together, there is significant blending of the emission features. Consequently, the derived parameters are unlikely to be reliable. Many structures that fall into this category are already well-known complexes such as W43 and W49.
6. Unclassified: this is a category for structures that cannot be classified as any of the types described above. An example of a structure that is included in this group is the Galactic centre region where the source density is so high that the algorithm is unable to identify individual structures and effectively groups all of the emission into a single enormous structure. This category is therefore not considered a distinct structure type and is excluded from further analysis.

In Fig. 4 we present a typical example of each of these classification types to illustrate some of the features discussed above. For each structure type we present the dust emission map and images of the mid-infrared emission. In many cases corresponding structures are seen in the infrared images and these can therefore provide strong support for the structures identified by `DisPerSE` and can assist in the classification, particularly when the dust emission is weak.

Cloud structures are complicated and difficult to categorise as they have irregular morphologies, and their boundaries are not well defined (e.g. Goldsmith et al. 2008; Williams et al. 2000). For these reasons a definitive classification of different types of structures is often not possible. The descriptions provided above are quite loose and the resulting classification can be somewhat subjective. To mitigate this, classifications have been made independently by five members of the team using the criteria given above. Only structures that have been given the same classification by three or more of the five leading authors are considered to be bona fide examples of each type. A similar method has been applied in a number of other studies, which have resulted in the production of reliable and representative samples of different types of Galactic structures (e.g. giant molecular filaments – Ragan et al. 2014, H II region bubbles – Churchwell et al. 2006 and extended green objects – Cyganowski et al. 2008).

3.2. Estimating sizes and total flux of structures

As discussed in the previous subsection, the algorithm traces the high column density structures by connecting regions of emission seen in the dust maps; the resulting skeletons essentially form the backbone of the structures and are referred to as the *source skeletons*. Although these source skeletons are useful and convenient to trace the underlying structures, they are not sufficient for estimating the angular sizes and the total flux associated with each structure. To achieve this we use an image processing operation called *dilation*[3]; this is a morphological operation that can be applied to binary images by expanding shapes contained in the input image with another structural element.

The structural element used in dilation is a box with both sizes of the same length. Our starting point is the source skeleton. When the square has a size of 1 pixel we are essentially just tracing the skeleton, but as we increase the size of the square we start to dilate the skeleton and incorporate more of the surrounding emission. In Fig. 2 we present an example of this method to illustrate the results of this process for different size squares. In general, a dilation operation with a square of size N (pixels) generates a *skeleton box* of width N (pixels). The challenge is to determine the optimum size of the square, in pixels, to use so that the majority of the flux associated with a structure is captured while avoiding possible contamination by unassociated nearby structures.

Two quantities can be readily defined with the help of the image dilation. Here, we define the integrated flux, $S_{\rm int}$, to the sum of all pixels contained in a skeleton box of width N as

$$S_{\rm int}(N) = \int_{w=N} I(x,y)\,{\rm d}x\,{\rm d}y, \tag{1}$$

where the integration is carried out inside the skeleton, and dx and dy are measured in pixels. Similarly, we can define the total number of pixels inside the skeleton of width N, which is denoted as $N_{\rm pixel}(N)$. The normalised intensity is then defined as:

$$I(N) = \frac{{\rm d}S_{\rm int}(N)}{{\rm d}N_{\rm pixel}(N)}. \tag{2}$$

[3] http://en.wikipedia.org/wiki/Dilation_(morphology)

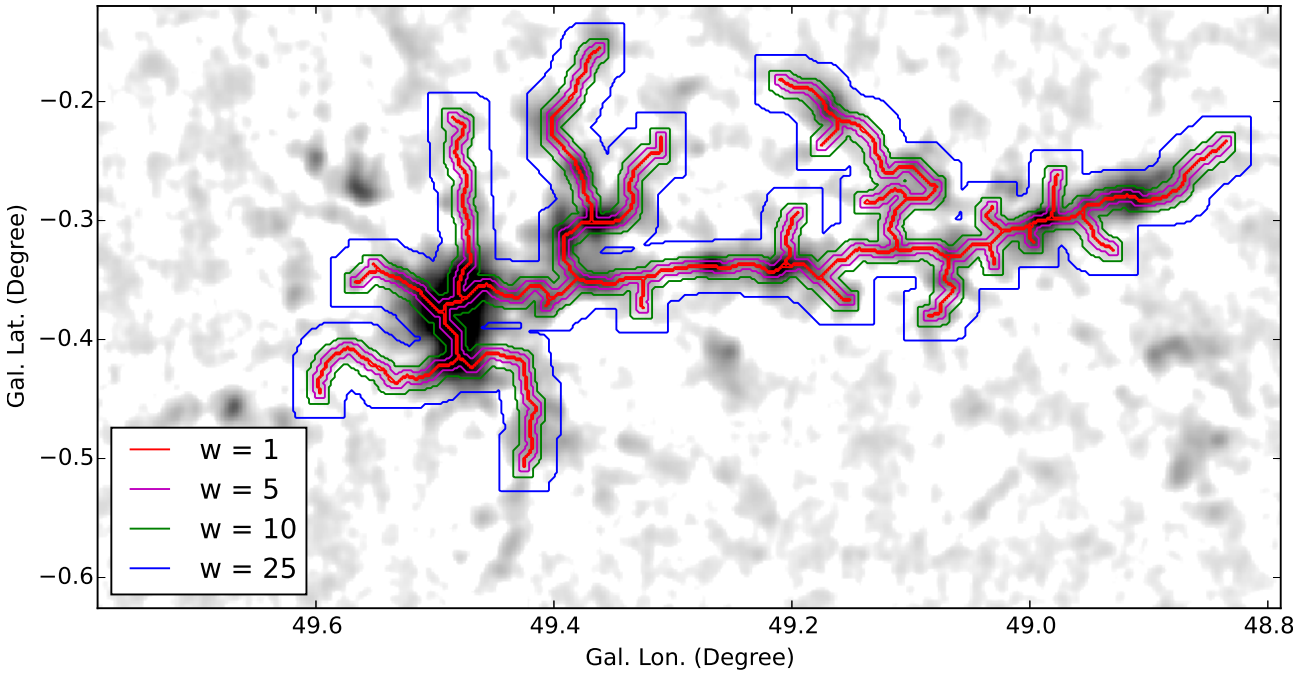

Fig. 2. Demonstration of the dilation operation applied to the source skeleton identified towards the W51 molecular cloud. The grayscale image shows the dust continuum emission mapped with ATLASGAL while surrounding contours show how the size and shape of the dilated skeleton changes as it is dilated by squares of increasing sizes. The red contour shows a dilation by a square of 1 pixel and simply traces the original skeleton as this also has a width of 1 pixel. The pink, green, blue contours show the structure after the original skeleton has been dilated with a square of width of w = 5, 10 and 25 pixels, respectively.

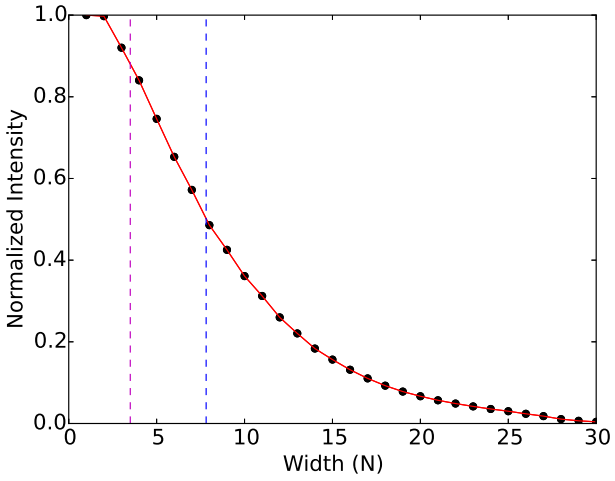

Fig. 3. Example of the normalized mean intensity as a function of the width of the dilated skeleton for W51. The filled circles show the measurements while the solid red line simply traces their distribution. The magenta and blue dashed vertical lines, respectively, indicate the angular resolution of the original ATLASGAL maps (19.2″ corresponding to ∼3.2 pixels) and the width of the structure, which is defined as the size at which the intensity reaches half of its maximum.

An important point to note is that while the identification of the structures has been performed on smoothed maps to improve the sensitivity to lower density connecting fragments, we have used the original higher resolution ATLASGAL emission maps to estimate their associated properties. In Fig. 3 we present the normalised pixel intensity as a function of increasing dilation width. It is clear from this plot that the peak flux density decreases with increasing distance from the emission ridge, which is traced by the skeleton. From inspection of the distribution shown in Fig. 3 and the example shown in Fig. 2 we estimate the optimum value for the skeleton box width is approximately 25 pixels; this width ensures that the vast majority of the fluxes are captured and that fluxes from pixels above 10% of the peak intensity are included. This is also the maximum angular scale that the ATLASGAL survey is sensitive to. We have therefore used this value to derive the dilated skeletons, which are subsequently used to estimate the total flux and to calculate the structure sizes and their orientations.

We estimate the width of each structure taking the point where the averaged intensity drops to half of its maximum (see the blue vertical line shown in Fig. 3). Note that our definition of the width differs from the definition commonly used in analysing *Herschel* observations (e.g. Arzoumanian et al. 2011; Men'shchikov et al. 2010) where they fit analytical formulae to the filament profiles obtained by stacking the maps based on the skeletons. We choose our dilation-based definition since we are interested in how gas concentrates around the skeleton, rather that studying the profiles in detail. Properties of the detected structures are presented in Table 1.

3.3. Catalogue of identified structures

Of the 1812 structures identified we find agreement for 1339 structures, which is approximately three-quarters of the sample and demonstrates the difficulties involved in classifying these types of objects. The situation is a little better than the statistics would suggest as many of the disagreements are for structures that fall between two similar types of structures e.g. when does an elongated structure become a filament and when does a filament with a number of sub-branches become a network? In this paper we have chosen to focus on the structures where the morphology is relatively unambiguous.

Table 1. Catalogue of ATLASGAL structures extracted by `DisPerSE` and identified as filaments by visual inspection of the emission maps.

Catalogue name (1)	Agreement flag (2)	ℓ (°) (3)	dℓ (°) (4)	b (°) (5)	db (°) (6)	$\sigma_{\rm maj}$ (′) (7)	$\sigma_{\rm min}$ (′) (8)	Aspect ratio (9)	θ (°) (10)	Width (″) (11)	$S_{\rm int}$ (Jy) (12)	nPixels (13)	nCSC (14)
G008.255+0.165	4	8.244	0.912	0.168	0.878	1.3	0.8	1.5	−86.6	32.1	15.4	74	3
G008.675−0.689	5	8.667	0.947	−0.692	0.865	2.1	0.5	4.0	−68.3	45.5	16.8	69	3
G008.800−0.359	4	8.807	0.895	−0.370	0.923	1.8	1.2	1.5	2.1	30.1	12.0	116	4
G008.914−0.318	4	8.914	0.978	−0.326	0.862	3.2	0.5	6.7	85.5	30.3	8.3	95	2
G009.230+0.157	4	9.234	0.898	0.146	0.868	1.3	0.6	2.3	−67.2	32.0	4.8	50	1
G009.280−0.152	4	9.280	0.870	−0.157	0.880	0.8	0.3	2.5	37.0	28.8	7.6	33	1
G009.541−0.664	4	9.544	0.928	−0.657	0.883	1.9	0.9	2.2	78.4	32.0	13.0	82	3
G009.853−0.739	4	9.812	1.077	−0.733	0.908	3.3	0.6	6.0	−72.8	35.1	62.3	171	7
G009.970−0.024	5	9.964	0.942	−0.026	0.865	1.6	0.4	3.7	−75.5	30.4	12.8	79	3
G010.531−0.024	3	10.538	0.928	−0.032	0.860	2.3	0.7	3.4	−82.6	31.0	6.0	66	2

Notes. The columns are as follows: (1) name derived from Galactic coordinates of the maximum intensity in the structure; (2) level of agreement; (3)–(6) Galactic coordinates of the emission centroid and the angular extent of the structure; (7)–(10) semi-major and semi-minor size, aspect ratio and source position angle measured anti-clockwise from Galactic mid-plane; (11) the width estimated from the normalized intensity distribution (e.g. Fig. 3); (12) integrated flux densities determined from the flux of all pixels found within the *skeleton box*; (13) number of connecting pixels that form the spine of the skeleton; (14) number of associated clumps identified in the ATLASGAL CSC. Only a small portion of the data is provided here, the full table is only available at the CDS.

In estimating the sizes, orientation and total flux associated with each structure we take all the pixels inside the $w = 25$ pixels mask into account (see Sect. 3.2) with a signal-to-noise ratio (S/N) >3. The size of the major and minor axes and their orientation is determined by diagonalizing the tensor of second moments of the position coordinates weighted by the pixel intensity. We define the major and minor sizes as the larger and smaller eigenvalue of the tensor, respectively, while the orientation as the angle between the larger eigenvector and the Galactic mid-plane.

In Table 1 we present the observed properties of the 517 filamentary structures identified. The structure names given in Col. 1 are based on the Galactic coordinates of flux weighted centroid position. In Cols. 2–5 we give the coordinates of the centroid position and angular size of each structure while in Cols. 6, 7 we give semi-major and semi-minor axis lengths that represent the standard deviation of the pixel co-ordinate values about the centroid position, weighted by the pixel values. The aspect ratio and the orientation of the structure, θ, is presented in Cols. 8 and 9 while in Col. 10 we give the width in arcsecs. In Cols. 11 and 12 we give the integrated 870 μm flux and number of pixels that define the spine of the structures. Finally, in Col. 13 we give the number of associated ATLASGAL Compact Source Catalogue (CSC; Contreras et al. 2013; Urquhart et al. 2014a), which will be discussed in more detail later in this section.

3.4. Properties of the various kinds of structures

The classification has been performed from a visual examination of the dust and mid-infrared images, however, we might expect the different structure types to have significantly different properties. In Fig. 5 we present plots showing the distributions of the number of pixels as a function of the aspect ratio (upper panel) and the semi-major and semi-minor axes (lower panel). The subsamples are well separated in the parameter space although we note there are still some significant overlaps. The complexes and networks appear to be well mixed with similar aspect ratios and numbers of pixels, and it might transpire that they are in fact similar kinds of structures with the complexes being more distant and active regions that are simply less well resolved in the ATLASGAL beam. These two types of structures are, however, relatively well separated from the filaments and elongated structures, which are themselves well separated from each other. Despite the difficulties associated with classifying these structures we do find that the different types of structures have fairly distinct properties and this provides strong reassurance that both the classification scheme and the method used are reliable.

In Table 2 we present the number of structures identified for each structure type along with the fraction of the total flux normalized with respect to the total flux in all the detected structures. Here we only included the 1339 structures for which we have agreement. A number of other statistical properties are also included. This table provides some immediate insights into the relative importance of the various kinds of structures identified. The combination of the marginally resolved and elongated structures contribute approximately 50% of the structures identified, but they only contribute a relatively small fraction of the total flux (~17%). The next most numerous structure type is the filaments, which contribute ~40% of the total number of structures, however, these contribute a disproportionate amount of the total flux given their number (~26%).

The majority of the flux (~37%) is associated with the filamentary networks, which themselves contribute approximately 10% of the structures. Combined with filaments we find that these kinds of structures make up approximately 50% of all identified sources and are associated with 60% of the total flux. If we assume that the different types of structures have a similar distance and temperature distribution, and there is no reason to think otherwise, then we can use the integrated fluxes as a proxy for the masses. Although this is likely to be somewhat imprecise it provides a useful ballpark estimate for the fraction of mass associated with each structure type. This crude analysis suggests that filaments and filamentary networks may also contribute roughly 60% of the mass associated with the identified structures. Furthermore, due to the limited resolution and sensitivity of the ATLASGAL survey it is likely that the fraction of filaments we have found is a lower limit. This highlights the ubiquitous nature of filamentary structures and their potential importance to current and future star formation in the Galaxy.

Complexes make up only 2% of the structures identified, however, given their size they still contribute a significant amount of the total flux, and therefore also the mass across the inner Galaxy (~22%). Many of the well know star

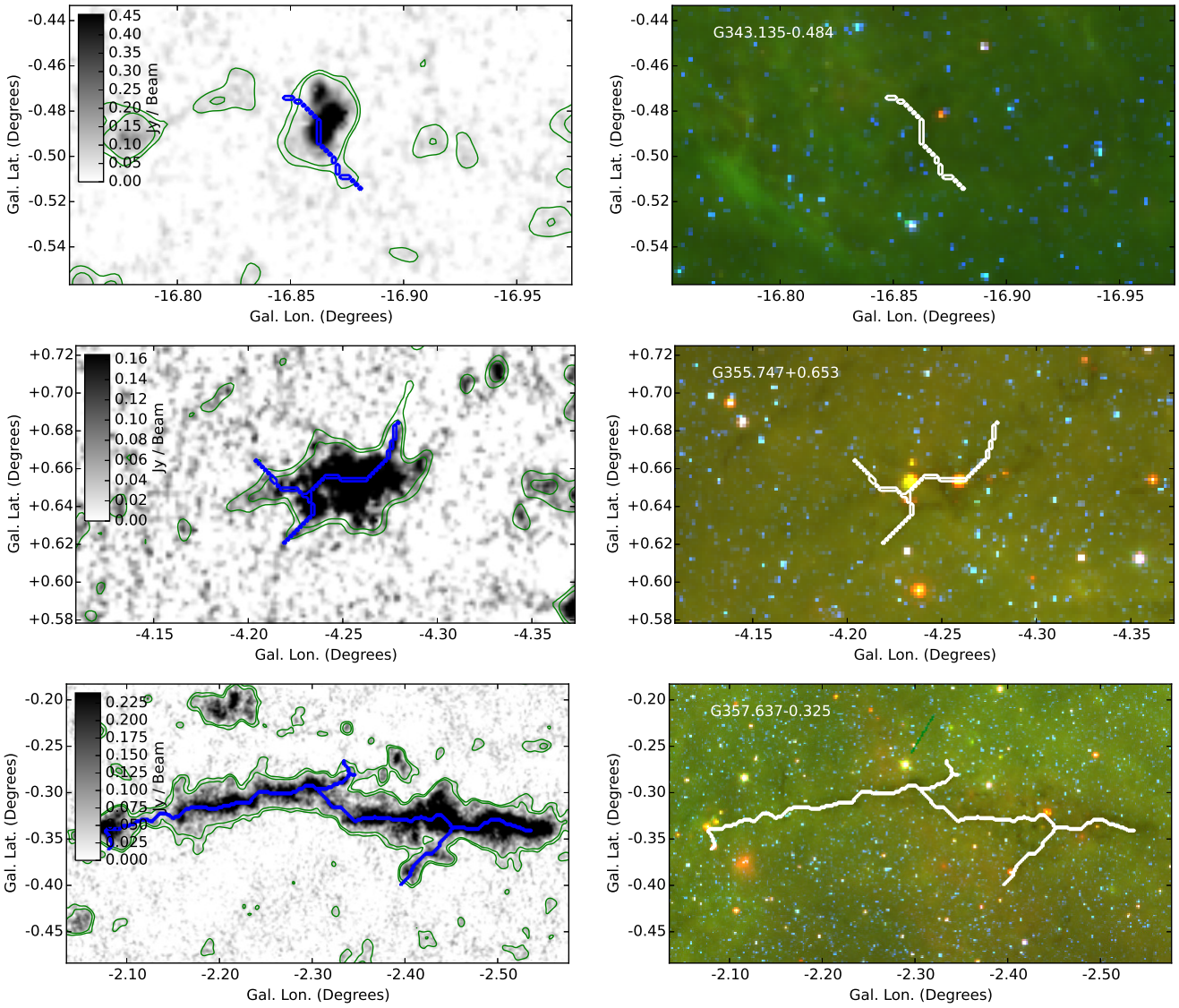

Fig. 4. Examples of the different structure types identified. The dust continuum images are presented in the *left hand panels* while in the *right hand panels* we present three colour composite mid-infrared images; they are produced using the 4.5, 8.0 μm IRAC bands taken from the GLIMPSE survey (Benjamin et al. 2003; Churchwell et al. 2009) and the 24 μm MIPS band image extracted from the MIPSGAL survey (Carey et al. 2005). The green contours show the 3 and 5σ noise levels. The blue and white lines overlaid on the *left and right panels* trace the skeletons of the structures identified by the `DisPerSE` algorithm. In the *upper, middle and lower panels* we show an example of an marginally resolved clumps, a marginally resolved elongated structure and a filament, respectively.

formation complexes belong to this group, such as W43, W49 and RCW106/G333. Altogether with the network of filaments we find that they contribute only 11% of the total number of structures but due to their sizes they are associated with ~60% of the total flux and likely to contain a similar fraction of the total mass found in these 1339 structures. This would suggest that much of the dense mass, and presumably also the star formation, is concentrated in a relatively small number of very large and massive structures. This is consistent with the findings of Murray & Rahman (2010) and Urquhart et al. (2014c) that a significant fraction (30–50%) of all of the Galactic star formation is concentrated in the most luminous 20–30 regions located in the Galactic mid-plane.

In Table 2 we also give the aspect ratio and the mean number of associated spine pixels. The aspect ratio is simply the ratio of the semi-major and semi-minor axes. As one would expect filaments have significantly larger aspect ratios than any of the other structure types, which is also clearly seen in Fig. 5. For the elongated structures and filaments the number of pixels can be used as a reasonable approximation of their observed length. Here again there is a clear trend for increasing numbers of pixels as we move from elongated structures to filaments and this is roughly correlated with the increasing aspect ratio for these structure types. However, this trend breaks down for networks and complexes as these tend to be associated with multiple intersecting filamentary structures. The structural complexity makes it difficult to provide reliable estimates of the lengths of these structures.

In Fig. 6 we show the cumulative distribution of the widths of the various structures. The properties have been extracted from the original maps and it is therefore clear from this plot that the widths of majority of structures are resolved by ATLASGAL. We also note that, with the exception of the marginally resolved

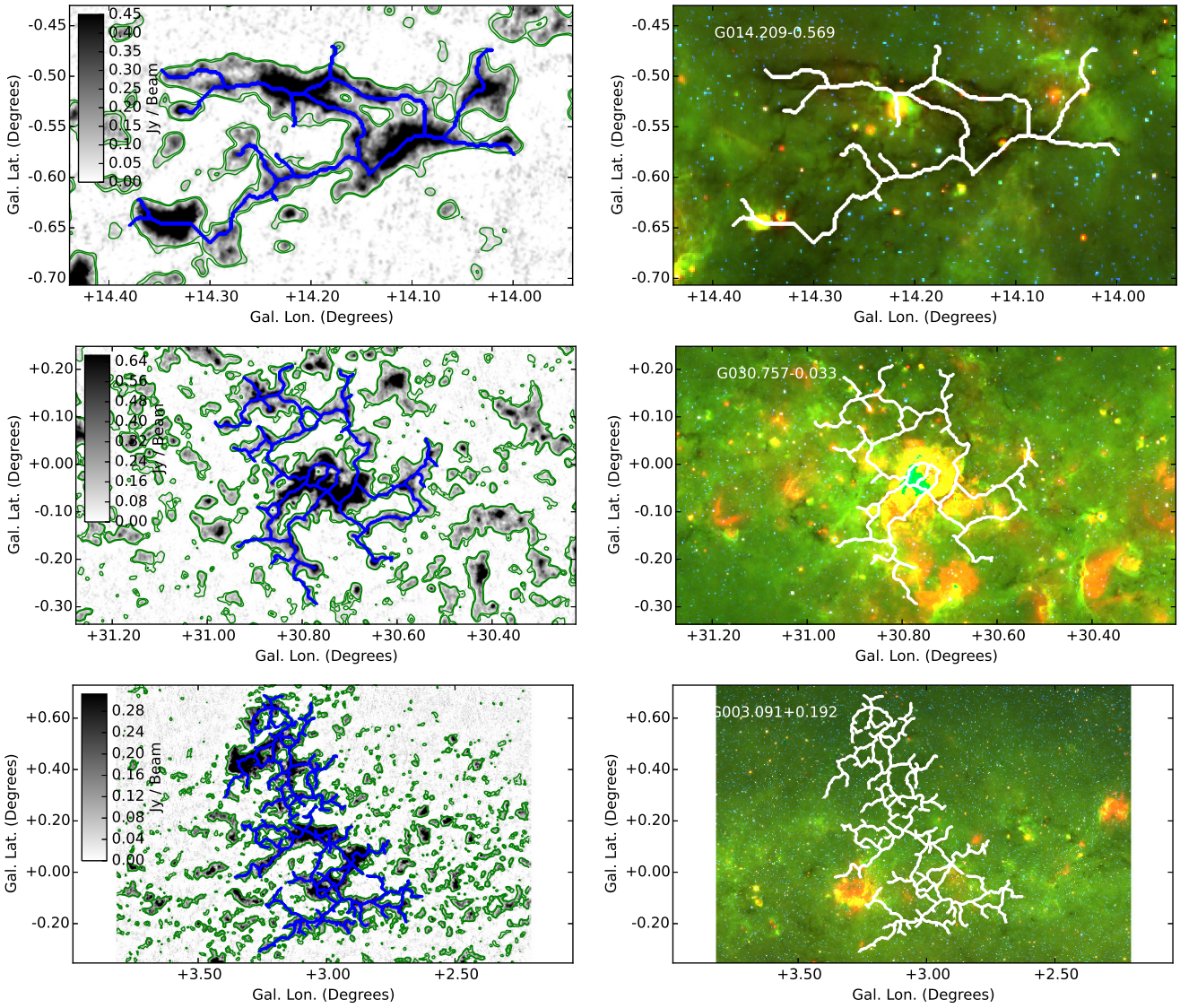

Fig. 4. continued. In the *upper, middle* we show an example of an network of filaments, a complex and an unclassified structure, respectively. Structures that are assigned as unclassified are excluded from further considerations.

Table 2. Summary of structure types and their statistical properties.

Structure type	Number	Fraction of structures	Fraction of total flux	Aspect ratio	Mean number of pixels	Total number of CSC assoc.	Mean number of CSC assoc.	Total number of MSF assoc.	Total number of MSF clumps	Fraction of MSF clumps
(1)	(2)	(3)	(4)	(5)	(6)	(7)	(8)	(9)	(10)	(11)
Clumps	370	0.28	0.06	2.09	44	325	0.9	11	12	0.02
Elongated	301	0.22	0.11	1.91	54	499	1.7	33	36	0.07
Filament	517	0.39	0.26	3.18	93	1495	2.9	43	63	0.12
Network	119	0.09	0.37	1.97	357	1609	13.5	29	80	0.15
Complex	32	0.02	0.21	1.81	444	574	17.9	9	32	0.06

Notes. The flux ratio is estimated by considering only the flux associated with structures where agreement is found. The fluxes are normalised with respect to the total flux in all the structures where agreement is found for the five main structure types. When determining the statistics for the association with the massive star forming (MSF) clumps we only consider structures outside of the inner 10° of the Galactic centre where the matching between ATLASGAL and massive star formation tracers is complete (for details see Urquhart et al. 2014c).

structures, the filaments have significantly narrower widths than the other structures. We will discuss the widths of the filaments in more detail in Sect. 4.4.

In Fig. 7 we show the distribution of the angle between the semi-major axis of the filaments and the Galactic plane for all structures with an aspect ratio larger than 3, the vast majority of which have been classified as filaments. We have chosen to restrict this analysis to the more elongated structures to minimise the uncertainty in the position angle. This plot reveals a broad but significant peak in the structure orientation with respect to the Galactic mid-plane with an angle of between 0 and 20°. This suggests that the elongated structures are preferentially aligned parallel to the plane of the Galaxy. This correlation is independent of their Galactic location i.e. we find no correlation

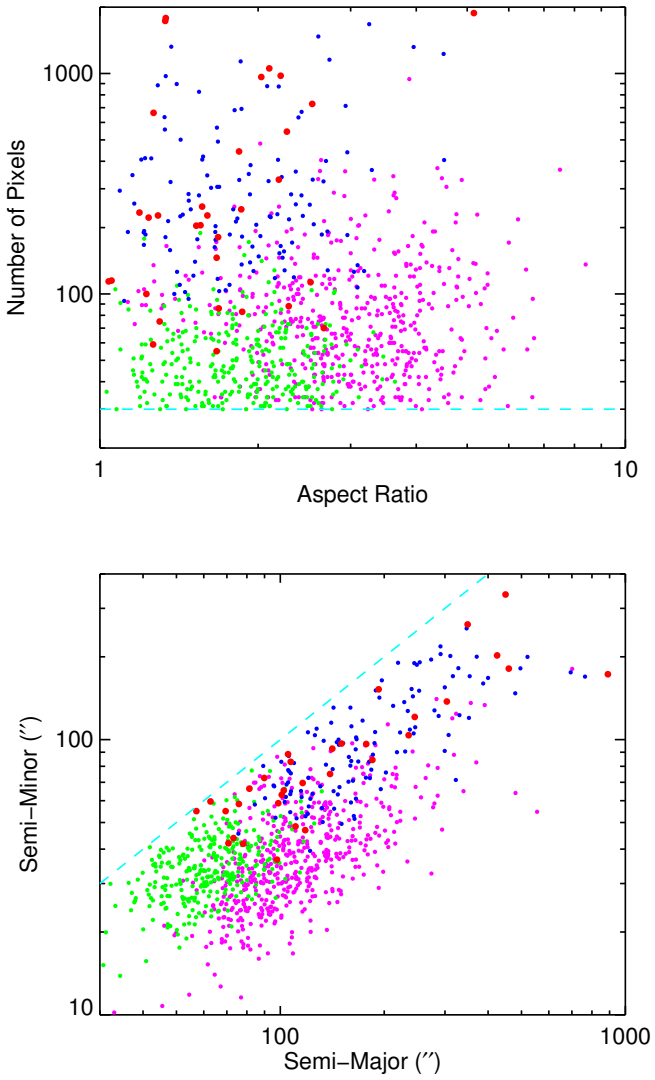

Fig. 5. Observed properties of the different structure types identified in Sect. 3. These plots show the distributions of angular sizes, number of associated spine points and shapes of the elongated structures, filaments, networks of filaments and complexes, which are shown as filled green, magenta, blue and red circles, respectively. For clarity we have excluded the marginally resolved structures as there is significant overlap with the elongated structures. The horizontal dashed line shown in the *upper panel* indicates the threshold of thirty pixels required for inclusion in the catalogue while the diagonal dashed line shown in the *lower panel* shows the line of equality where the semi-major and semi-minor axes are equal.

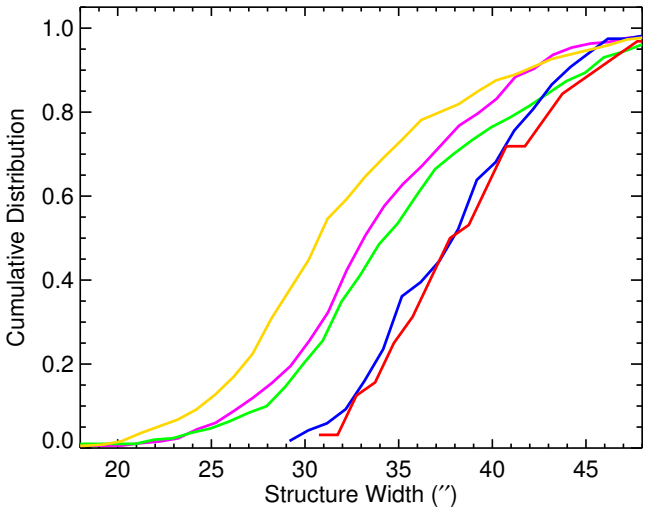

Fig. 6. Cumulative distribution of the pixel widths of each type of structure. The yellow, green, magenta, blue and red curves show the distribution of marginally resolved, elongated structures, filaments, networks of filaments and complexes, respectively.

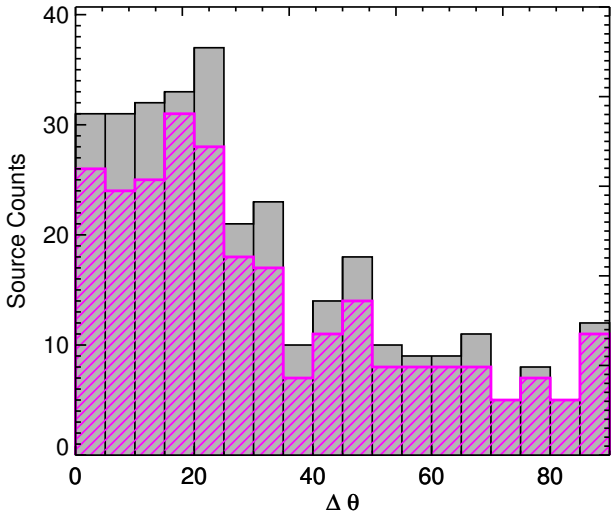

Fig. 7. Angle between the semi-major axis of the filaments and the Galactic plane. The results of all structures with an aspect ratio greater than 3 are shown as a grey histogram while those classified as filaments are shown in magenta.

between the orientation of the and Galactic longitude or angular separation from the mid-plane (i.e. $|b|$). We will investigate this correlation in more detail in Sect. 5.2.

3.5. Association with ATLASGAL Compact Source Catalogue

In the following, we match the sample with the ATLASGAL Compact Source Catalogue (CSC; Contreras et al. 2013; Urquhart et al. 2014a)[4], which was produced using the SExtractor algorithm (Bertin & Arnouts 1996). A useful output produced by this extraction code are image masks. They are the same size and dimensions as the input emission maps but each pixel is given an integer value that relates each pixel to a source in the catalogue. These masks therefore contain the emission footprint of each source and by mapping the spine positions onto these maps we can unambiguously identify associations between the CSC and structures identified by DisPerSE, which in turn can provide some insight into source sub-structure. Furthermore, making the link between the structures and the CSC allows us to assign velocities and distances to many of the structures that have been determined from previous work by the ATLASGAL team (e.g. Wienen et al. 2012, 2015; Urquhart et al. 2014c; König et al. 2015) and from the literature (e.g. Ellsworth-Bowers et al. 2015; Green & McClure-Griffiths 2011; Dunham et al. 2011b; Schlingman et al. 2011; Roman-Duval et al. 2009).

[4] http://atlasgal.mpifr-bonn.mpg.de/cgi-bin/ATLASGAL_DATABASE.cgi

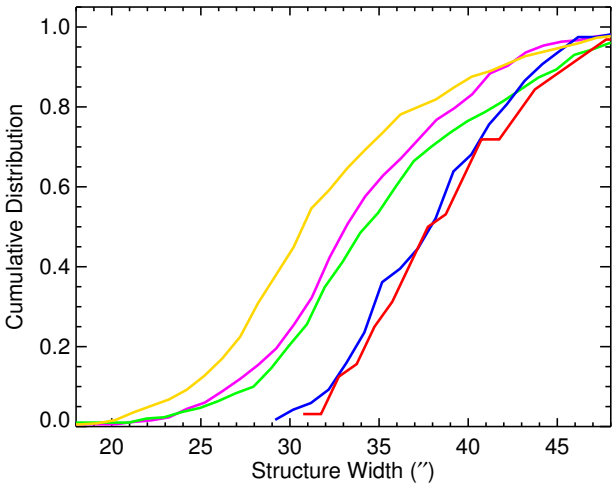

Fig. 8. Cumulative distribution showing the fraction of the various types of structures with a particular integer number of CSC or few associations. The green, magenta, red and blue show the distributions of the elongated structures and filaments and complexes and networks of filaments, respectively.

The compact source catalogue derived from the ATALSGAL survey provided an unbiased view of the distribution of dense gas (i.e. $>\sim10^{22}$ cm^{-2}) in the Galaxy (Schuller et al. 2009). We find that roughly two-thirds of the structures where agreement is found are associated with one or more ATLASGAL CSC, with an average of four clumps being associated with each structure (4502 ATLASGAL CSC associated with 1042 structures). A full breakdown of the structures and the number of associations is given in Table 2. In Fig. 8 we present a cumulative distribution plot showing the fraction of structures as a function of the number of CSC associations. As one would expect the mean number of CSC associations increases with the complexity of the structure, with marginally resolved structures being associated with an average of ∼1 compact clump while filaments are associated with an average of 3 clumps and complexes with an average of ∼20 dense clumps; these values are relatively unaffected if we exclude the Galactic centre region (i.e. $|\ell| < 10°$).

Previous work has been done to match dense clumps in the ATLASGAL CSC with signposts of massive star formation. In a recent series of papers Urquhart et al. (2013a,b, 2014c) identified a large sample of massive star forming (MSF) clumps by associating ATLASGAL clumps with methanol masers identified by the methanol multibeam (MMB; Green 2009), which are considered to be an excellent tracers of massive star formation (e.g. Walsh et al. 1998; Minier et al. 2003), mid-infrared bright massive young stellar objects (MYSOs) identified by the Red MSX Source (RMS) survey (Lumsden et al. 2013) and compact and ultracompact H II regions identified by both the RMS and CORNISH (Hoare et al. 2012; Purcell et al. 2013) surveys. In total some ∼1300 MSF clumps have been identified, however, two of the three surveys used for the matching exclude the inner ten degrees of the Galactic plane. The MSF associated sample of clumps also includes the ATLASGAL-Extension region (ℓ = 280–300° and b = −2 to 1°), which is not considered in this work. The total number of MSF in the area of interest considered here is 981, of which we find 520 are associated with structures where agreement is found; this corresponds to approximately 53% of the MSF associated clumps.

Comparing the fraction of MSF clumps associated with each type of structure (Cols. 4 and 11 in Table 2) we find it is tightly correlated with the fraction of the total flux associated with these structure types. Both the flux and fraction of MSF clumps agree within a few percent. It would therefore appear that the number of MSF sites associated with any type of structure is roughly proportional to the amount of dense material associated with them, which indicates that these gas condensations share a similar structure at the clump scale.

4. Properties of the filaments

The primary motivation for this paper is to produce a representative catalogue of filamentary structures and therefore the rest of the paper we will focus exclusively on the 517 of these structures identified in the previous section; for brevity we will refer to these as filaments but note that these may be physically distinct structures from other "filaments" discussed in the literature[5]. Several examples of filaments are presented in Fig. 9. We do not consider the networks of filaments as they are rather more complicated and their properties are more difficult to determine and somewhat less reliable. In Table 1 we present the structure names and physical properties derived in this section. Of these, 130 filaments were agreed on by three reviewers, 160 were agreed on by 4 reviewers, and 227 filaments were unanimously agreed upon. These can be considered as a crude confidence flag and so we include this information in Table 1 where the integer values of 3, 4 and 5 indicate the level of agreement for the filaments with a 5 considered to have the highest reliability.

Given the sensitivity and limited spatial resolution of the ATLASGAL survey this catalogue of filamentary structures is unlikely to be complete. However, given the unbiased nature of the ATLASGAL survey and the systematic way the filaments have been identified this sample is likely to be representative of a particular size and mass not previously well studied in literature. This sample therefore represents a significant advance on what was previously known (see Sect. 5.1 for a thorough discussion.)

4.1. Integrated flux distribution

The filaments are associated with 1495 CSC sources with an average of three clumps being associated with each filament. There are, however, some 96 filaments that do not have any counterparts in the CSC. In Fig. 10 we present the integrated flux distribution for the whole filament sample (grey histogram) and those associated with one or more ATLASGAL CSC sources (yellow hatched histogram). Is it clear from this plot that the filaments that are not associated with any compact sources have significantly lower fluxes. It is likely these have only become detectable in the smoothed maps used with `DisPerSE` to identify large structures.

A consequence of this is that there is little complementary data available for these weaker filament. However, these may be more distant examples of these types of structures or may simply be lower density nearby filaments. The mean aspect ratios of the filaments associated and unassociated with CSC sources is not significantly different. However, the latter are associated with approximately half as many spine pixels and so are generally smaller, which is consistent with what we would expect if they are more distant examples of the same type of structures. If this is indeed the case then the analysis of the 421 filaments that are associated with CSC sources should produce statistically robust

[5] The full catalogue and the corresponding data files are available at `http://atlasgal.mpifr-bonn.mpg.de/cgi-bin/ATLASGAL_FILAMENTS.cgi`

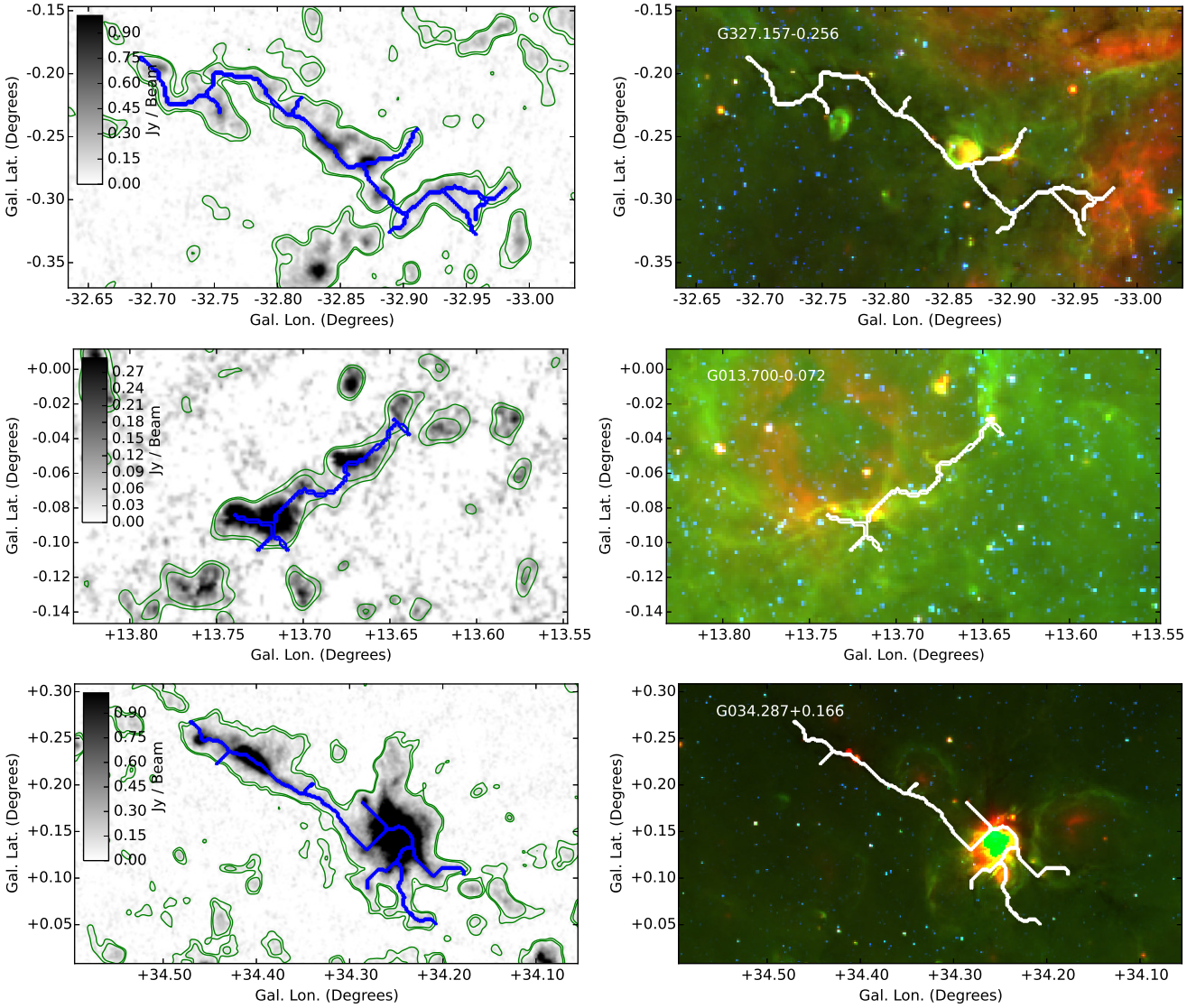

Fig. 9. Examples of filaments. For image details see caption of Fig. 4.

results, as these structures are expected to be representative of the whole sample.

4.2. Radial velocities

In the following analysis we will only consider the sample of 421 filaments associated with ATLASGAL clumps as velocities and distances are available for a large fraction of these from both our own programmes of follow-up molecular line observations (Wienen et al. 2012, 2015; Giannetti et al. 2014; Csengeri et al. 2016a), and from the results of other large-scale line surveys previously mentioned. These observations are directed towards the peak intensity region found towards the of the dense clumps. This data is heterogeneous as transitions from various molecules with different critical densities are used to determine the velocities. However, a large proportion have high critical densities such as CS (2–1) and NH_3 (1,1) that are able to unambiguously identify the correct radial velocities of the clumps; when available they are preferred over CO measurements that are also sensitive to low density diffuse clouds, which can lead to multiple velocity components being detected along the line of sight.

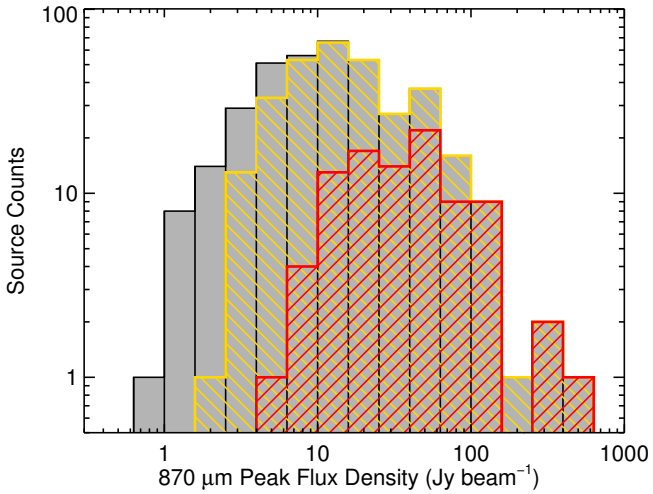

Fig. 10. Integrated flux distribution of all filaments is shown by the grey histogram while the yellow hatched histogram shows only those associated with one or more ATLASGAL CSC sources. The red hatched histogram shows the flux distribution of the filaments that are associated with massive star forming clumps.

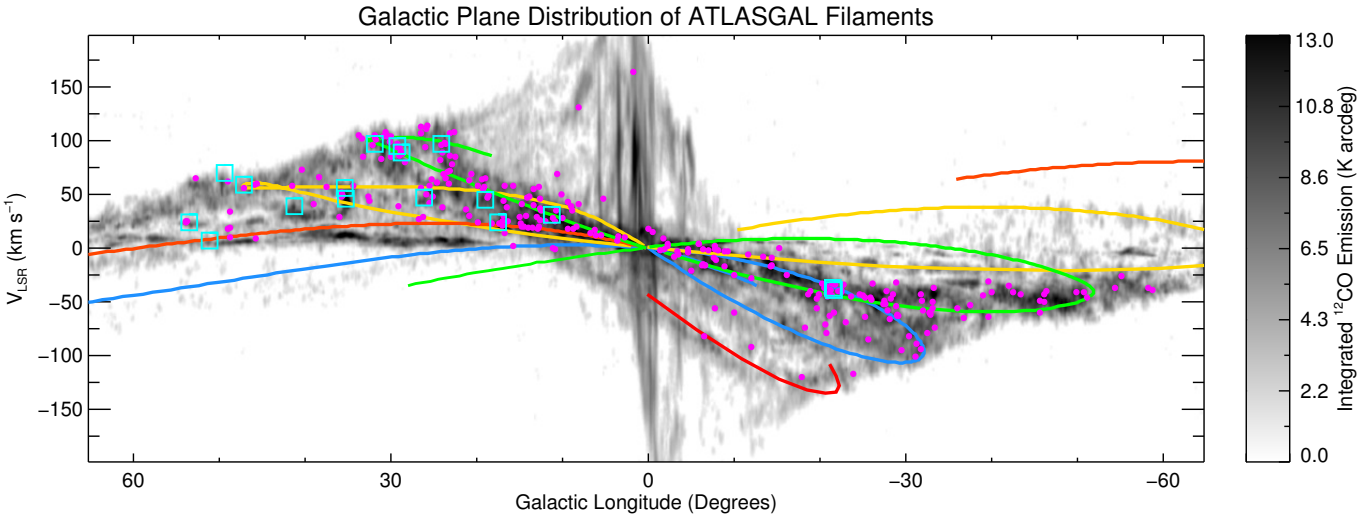

Fig. 11. Galactic longitude-velocity distribution of all filaments. The background image shows the distribution of molecular gas as traced by the integrated ^{12}CO (1-0) emission (Dame et al. 2001); the colour bar on the right shows the relative intensity of the emission. The magenta circles mark the positions of the ATLASGAL filaments while the cyan squares show the positions of other filamentary structures reported in the literatures (see Sect. 5.1 for details). The coloured lines trace the location of the spiral arms taken from the model by Taylor & Cordes (1993) and updated by Cordes (2004). The blue, green, yellow and orange curves trace the Norma, Scutum-Centaurus, Sagittarius and Perseus arms, which are the four main spiral arms, while the red curve tracers the Near 3-kpc expanding arm (Bronfman et al. 2000).

We have matched the results of these line observations with compact sources identified in the CSC and by association we are able to obtain velocity measurements to 310 filaments. Furthermore, since many of the filaments (230) are associated with multiple clumps with independent velocity measurements we are able to distinguish between filaments that have a coherent velocity from those that are likely the result from blending of different structures along the line of sight. Looking at these velocity measurements we find there are 31 structures with a standard deviation >10 km s^{-1}, the majority of these are likely to be chance alignment and can be rejected from the catalogue. Although some of these filaments may be broadly coherent in velocity with relatively little line of sight contamination, we prefer to be conservative and exclude them. It is likely that there are still some structures in the sample that are the result of chance alignments, however, statistical analysis suggests that this is likely to be a relatively small fraction. Poisson counting statistics suggests this number is ∼11 or 4% of the remaining sample of 279 filaments for which we have a velocity, which means that they are unlikely to have a significant impact on our analysis.

In Fig. 11 we present a plot of the Galactic longitude and velocity distribution of the filaments overlaid on the large-scale distribution of molecular gas as traced by the integrated ^{12}CO map of Dame et al. (2001), along with the positions of the four main spiral arms as determined by Taylor & Cordes (1993) and the 3-kpc expanding arm from Bronfman et al. (2000). The positions of the filaments appear to be tightly correlated with the loci of the spiral arms. For comparison we overlay a number of large-scale filamentary structures reported in the literature on Fig. 11. We will investigate this correlation in more detail in Sect. 5.3.

There are 111 filaments for which we have no velocity information. Of these, 54 are located towards the Galactic Centre (i.e. 350° < ℓ < 10°), which is an area that many molecular line studies have avoided, partly due to complexity of emission in this region, and partly because kinematically derived distances are unreliable. Of the remaining filaments all but 8 are located in the southern Galactic plane where the coverage by molecular line surveys is significantly poorer. Of the 315 filaments located outside the Galactic centre region we have assigned velocities to 258 (∼82%).

4.3. Distances

After excluding the filaments with a velocity dispersion greater than 10 km s^{-1} our sample is reduced to 279 filaments with available velocity information. In order to estimate values of the physical properties such as masses and sizes of the filaments we first need to determine their distances. There has been a number of recent dedicated Galactic plane survey datasets that have focused on determining distances to star forming regions (e.g. ATLASGAL – Wienen et al. 2015; Urquhart et al., in prep.; the Red MSX Survey (RMS) – Urquhart et al. 2014b; Bolocam Galactic Plane Survey (BGPS) – Dunham et al. 2011a; Ellsworth-Bowers et al. 2015; Battisti & Heyer 2014; H II region Discovery Survey (HRDS) – Bania et al. 2010 and the Galactic Ring Survey (GRS; Jackson et al. 2006) – Roman-Duval et al. 2009). The majority of these use the radial velocities of sources, obtained from molecular line observations, with a Galactic rotation curve to estimate the kinematic distances. For sources located within the Solar Circle the rotation curves return two possible distances, equally spaced on either side of the tangent position; they are commonly referred to as the *near* and *far* kinematic distances. This distance ambiguity is normally resolved by comparing the source velocity with the H I profile taken towards the source; this technique is known as the H I self-absorption method (for a more detailed discussion of this method see Jackson et al. 2002 and Roman-Duval et al. 2009). This is not the only method but it is the most commonly used and the only one relevant for the studies we have used to assign distances to our sample of filaments.

We estimate the systemic velocity from the average velocity of their associated clumps and use this to determine the near and far distances using the Brand & Blitz (1993) rotation model. We then resolve any distance ambiguities using the information given in the literature. We do not assign kinematic distances to structures with radial velocities close to the solar velocity (i.e.

Table 3. Physical properties of the 279 ATLASGAL filaments for which a velocity has been determined.

Structure name (1)	V_{LSR} (km s^{-1}) (3)	(Ref.) (4)	Distance (kpc) (5)	(Ref.) (6)	Length (pc) (7)	Width (pc) (8)	Log(Total Mass) ($M_\odot$) (9)	Log(Mean N_{H_2}) (cm^{-2}) (10)	Log(Peak N_{H_2}) (cm^{-2}) (11)	IRDC assoc. (12)	Bubble assoc. (13)
G001.653+0.203	163.2	1	···	···	···	···	···	21.52	21.74	···	···
G003.456+0.006	5.8	1	···	···	···	···	···	21.60	21.76	···	···
G005.101−0.104	45.4	2	2.8	1	5.03	0.40	3.176	21.56	21.76	···	···
G005.357+0.101	11.1	2, 3	3.0	1	2.58	0.41	2.802	21.63	21.88	···	···
G005.938−1.274	11.1	3	2.9	Near	4.50	0.13	3.495	21.87	22.08	···	···
G006.104−0.623	15.7	2, 3	3.7	1	6.10	0.62	3.705	21.71	21.87	···	···
G006.589−0.106	12.8	3	3.4	1	5.48	0.57	3.849	21.82	22.13	···	···
G008.000−0.272	39.9	4	11.8	1	9.13	1.60	4.373	21.74	22.04	···	···
G008.003−0.507	130.4	4	8.4	Tangent	6.41	1.00	3.560	21.65	21.78	···	···
G008.255+0.165	18.8	4	3.0	2, 3	2.25	0.38	3.090	21.59	21.93	···	···

Notes. Only a small portion of the data is provided here, the full table is only available at the CDS.

References. Velocity references: (1) Purcell et al. (2012); (2) Jackson et al. (2013); (3) Wienen et al. (2012); (4) Dunham et al. (2011a); (5) Shirley et al. (2013); (6) Bronfman et al. (1996); (7) Csengeri et al. (2016b); (8) Urquhart et al. (2011); (9) Urquhart et al. (2008); (10) Dempsey et al. (2013); (11) Wienen et al. (2016); (12) Rigby et al. (2016); (13) Urquhart et al. (2007); (14) Jackson et al. (2008); (15) Wyrowski et al. (in prep.); (16) Urquhart et al. (2014b); (17) Urquhart et al. (in prep.) Distance references: (1) Wienen et al. (2015); (2) Ellsworth-Bowers et al. (2013); (3) Dunham et al. (2011a); (4) Urquhart et al. (in prep.); (5) Urquhart et al. (2014a); (6) Roman-Duval et al. (2009); (7) Battisti & Heyer (2014); (8) Urquhart et al. (2014b); (9) Davies et al. (2012); (10) Reid et al. (2014).

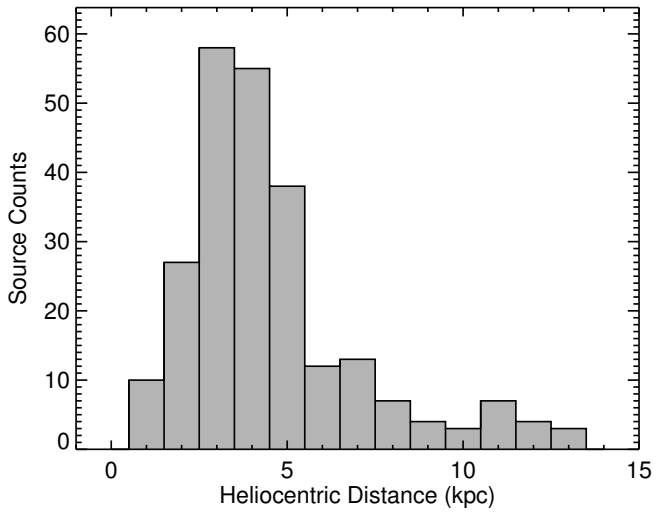

Fig. 12. Distance distribution. The bin size used is 1 kpc.

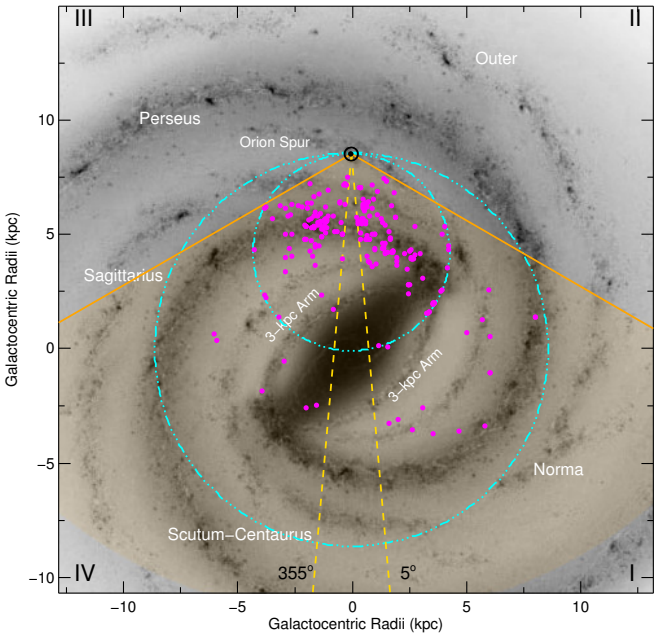

Fig. 13. Galactic distribution of all ATLASGAL filaments for which a distance has been determined. The orange shaded area indicates the region of the Galactic plane covered by the ATLASGAL survey to a distance of 20 kpc, within which the survey is complete for compact clumps with masses >1000 $M_\odot$. The background image is a schematic of the Galactic disk as viewed from the Northern Galactic Pole (courtesy of NASA/JPL-Caltech/R. Hurt (SSC/Caltech)). The Sun is located at the apex of the wedge and is indicated by the ⊙ symbol. The smaller of the two cyan dot-dashed circles represent the locus of tangent points, while the larger circle traces the Solar Circle. The spiral arms are labelled in white and Galactic quadrants are given by the roman numerals in the corners of the image. The yellow lines shows the innermost region towards the Galactic centre where distances are not reliable.

$|V_{LSR}| < 10$ km s^{-1}) as they are unreliable; this affects 30 filaments, however, maser parallax measurements are available for 4 of these filaments and reliable distances for another 2 of these can be found in the literature. We have been able to determine distances to 241 filaments from the various H I studies; the assigned distance and literature reference are given in Cols. 4 and 5 of Table 3. In Fig. 12 we present a histogram showing the distribution of heliocentric distances.

In Fig. 13 we show the Galactic distribution of the filaments overlaid on a schematic diagram of the Milky Way that includes many of the key elements of Galactic structure, such as the location of the spiral arms and the Galactic long and short bars (Churchwell et al. 2009). Comparing the distribution of the filaments with the spiral arms it is clear that the majority are associated with the near side of the Scutum-Centaurus arm that fills a large proportion of inner Galactic plane and has a heliocentric distance of ∼4 kpc. There is reasonable correlation between the filaments not associated with the Scutum-Centaurus arm and the other arms, however, the sampling is too sparse to draw any conclusions from this correlation. It is a little surprising that there are so few associations with the Sagittarius arm since it is the closest arm to us and covers a larger ℓ range. This is likely to be related to the removal to large angular scales in the data

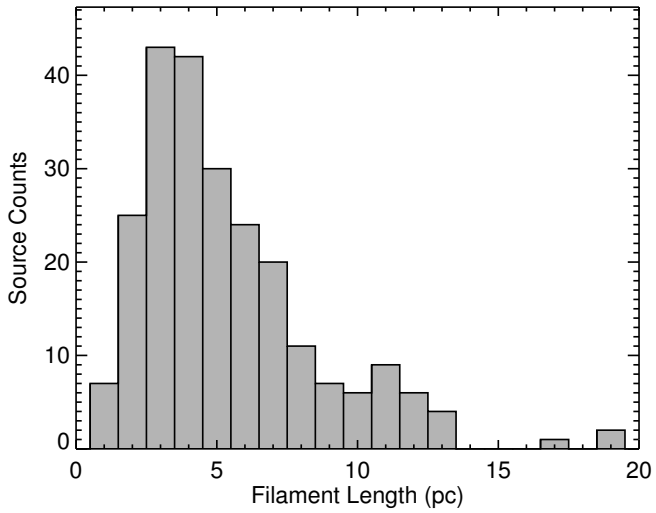

Fig. 14. Distribution of filament lengths as estimated from the angular size of the major axis. The bin size used is 1 pc.

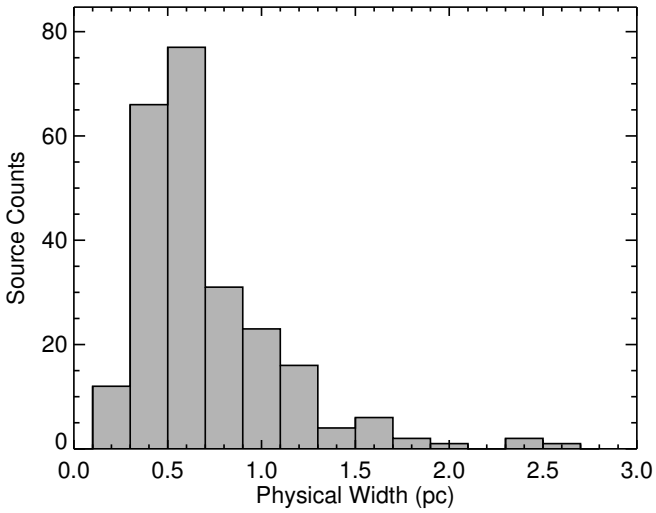

Fig. 15. Width distribution for 241 resolved filaments. The widths are determined from the original resolution maps, which have a resolution of 19.2″ derived from the APEX beam. The bin size used is 0.2 pc.

reduction process, decreasing our sensitivity to nearby extended low-density structures (as discussed in Sect. 2.1). We also note that while this spiral arm covers a large portion of the sky it falls outside the dense ring of material found towards the inner part of the Galaxy (i.e. the 4–5 kpc ring where ∼70% of the molecular gas in the Galaxy is found; Jackson et al. 2006) and therefore this part of the Sagittarius arm has a lower mass surface density so perhaps we might expect to find few filaments anyway. We will investigate the Galactic distribution in more detail in Sect. 5.3.

4.4. Lengths and widths

There are two possible methods we can use to estimate the length of a filament: the number of points that form the source skeleton or the length of the major axis. The former is likely to overestimate the length for structures with numerous sub-branches, while the latter is likely to underestimate the true length as it makes no allowance for any curvature that might be present in the source structure. We have opted to use the major axis as a measure of the physical length of filaments as this is easy to define and the results relatively easy to reproduce. Furthermore, although sizes are likely to be underestimated this is likely to be less of a problem for structures with large aspect ratios. In Fig. 14 we show the length distribution of the filaments and give the statistical breakdown in Table 4. Considering only filaments with an aspect ratio greater than 3 we estimate the range of lengths to be between ∼2 and 20 pc with a median value of 3.8 pc. This is similar to the lengths reported in a recent *Herschel*-HIGAL study of the $\ell = 216.5{-}225.5°$ region presented by Schisano et al. (2014). The lengths of many filaments in our sample are significantly smaller than some of the large-scale filaments that have recently been reported in the literature (e.g. Ragan et al. 2014; Li et al. 2013; Jackson et al. 2010), which have lengths of several tens to hundreds of parsecs (this will be discussed in detail in Sect. 5.1).

In Fig. 15 we show the distribution of widths for all resolved filaments. The median width is ∼0.5 pc, which is significantly larger than the widths measured from the *Herschel* Gould Belt Survey (André et al. 2014) where filament inner widths of ∼0.1 pc are typically reported for nearby clouds (e.g. Arzoumanian et al. 2011; Hill et al. 2012), and we have made no attempt to separate out the contribution from a possible power-low component (Palmeirim et al. 2013). Our measurements are in line with what has been found for other filaments found towards the inner Galaxy, (e.g. "Nessie" has a width of 0.5 pc – Jackson et al. 2010; and the "Snake" has a width of 0.8 pc – Wang et al. 2014), the widths of ∼0.3 reported by Schisano et al. 2014 and the range reported by Wang et al. (2015, 0.6–3 pc) for a sample of 9 *large-scale filaments*. However, we note that the values calculated here show a distance-dependence, i.e. we tend to find filaments with larger widths at larger distances (cf. Schisano et al. 2014).

We also note that while the major axis length is likely to underestimate the length of the filaments the minor axis is likely to overestimate their widths. The widths presented here provides an estimate of how concentrated the emission is with regards to the skeleton, but these parameters are not particularly well constrained by our data and should be considered to be upper limits and used with caution.

4.5. Masses, column densities and mass-to-length ratios

We estimate the mass of the filaments using the total integrated flux from the dilation operation described in Sect. 3.2 and following the method described by Hildebrand (1983)

$$M_{\rm filament} = \frac{D^2\, S_\nu\, R}{B_\nu(T_{\rm dust})\,\kappa_\nu}, \tag{3}$$

where S_ν is the integrated 870 μm flux, D is the heliocentric distance to the source, R is the gas-to-dust mass ratio (assumed to be 100), B_ν is the Planck function for a dust temperature $T_{\rm dust}$, and κ_ν is the dust absorption coefficient taken as 1.85 cm^2 g^{-1}; this values was interpolated by Schuller et al. (2009) from Table 1, Col. 5 of Ossenkopf & Henning (1994). In this calculation we are assuming that the total filament mass is proportional to the total flux density integrated over the source. In previous studies we have used temperatures of 18 K and 20 K when estimating the masses (e.g. Csengeri et al. 2014; Urquhart et al. 2014a). However, these were based on temperature measurements made towards the peaks of the submillimetre emission, which are often associated with star formation and therefore tend to be a little warmer than the temperature of their extended envelope. Here we assume a dust temperature of 15 K, which is more typical of

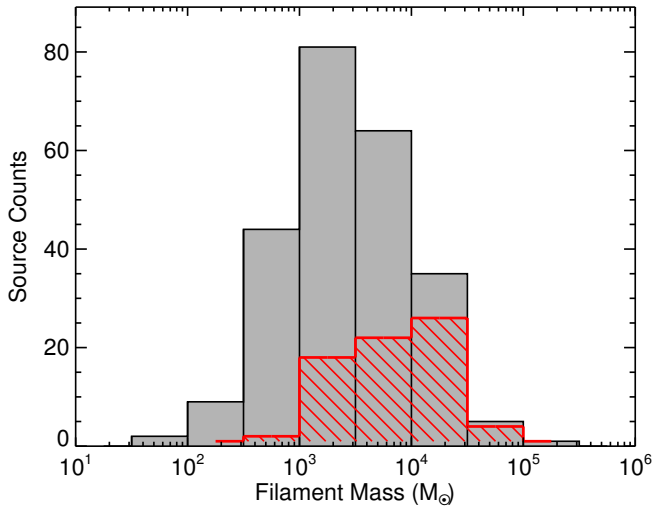

Fig. 16. The mass distribution of all filaments is shown in grey and is overlaid with the mass distribution of filaments associated with MSF (massive star forming) clumps in red. The bin size used is 0.5 dex.

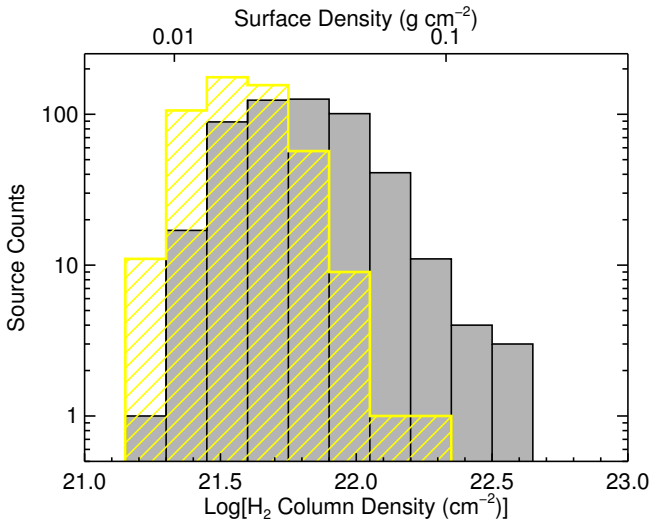

Fig. 17. Log-normal column density distribution. The filled grey histogram shows the peak column density of the skeleton pixels while the hatched yellow histogram shows the mean column density of all pixels associated with each filament. The bin size used is 0.15 dex.

the temperatures reported for IRDCs and quiescent clumps (e.g. Wienen et al. 2012; Urquhart et al. 2015). Using this temperature the equation simplifies to

$$\left(\frac{M_{\rm filament}}{M_\odot}\right) = 8.63 \left(\frac{D}{\rm kpc}\right)^2 \left(\frac{S_{\rm int}}{\rm Jy}\right). \quad (4)$$

In Fig. 16 we show the filament mass distribution. The filaments have masses from ∼100 $M_\odot$ to 10^5 $M_\odot$ with typical values of a few 1000 $M_\odot$, which is typical of the mass reservoir often associated with massive star formation. We also show the distribution of the filaments that are associated with massive star formation (Sect. 3.5). We use the Kolmogorov-Smirnov test (Press et al. 1992) to determine if the mass distribution of the MSF and non-MSF filaments are significantly different from each other. This test starts with the null hypothesis that both samples are drawn from the same parent population and this is rejected if this probability is less than 0.0013 (i.e. more than 3σ); this is known as the p-value. Comparing the masses are able to reject the null hypothesis with p-value $\ll$0.0013 and so the difference in mass is statistically significant.

To estimate the column density, following previous works (e.g. Schuller et al. 2009; Csengeri et al. 2014), we use

$$N({\rm H_2}) = \frac{S_\nu\, R}{B_\nu(T_{\rm dust})\, \Omega\, \kappa_\nu\, \mu_{\rm H_2}\, m_{\rm H}}, \quad (5)$$

where Ω is the beam solid angle, $\mu_{\rm H_2}$ is the mean molecular weight of the interstellar medium with respect to hydrogen molecules, which is equal to 2.8 (Kauffmann et al. 2008), and $m_{\rm H}$ is the mass of an hydrogen atom. The other parameters are as previously described. Again assuming a dust temperature of 15 K, the conversion between flux and column density can be expressed as

$$\left(\frac{N({\rm H_2})}{\rm cm^{-2}}\right) = 3.92 \times 10^{22}\, \frac{S_\nu}{\rm Jy/beam}. \quad (6)$$

In Fig. 17 we show peak and mean column density distributions. The peak column densities of the filament are determined by fitting a log-normal function to the distributions of column densities on pixels that form the spine of the source skeleton; and the mean column densities of the filaments are determined by fitting a log-normal function to the distribution of column densities of all pixels found within the dilated skeleton (i.e. w = 25 pixel). The average column densities of the filaments range between ∼2–13 × 10^{21} cm^{-2} with mean value of 3.55 × 10^{21} cm^{-2}. This is almost an order of magnitude higher than the mean value determined for the catalogue of filaments reported by Schisano et al. (2014, 1.7–4.8 × 10^{20} cm^{-2}) and explains how they were able to identify a similar number of filaments from a relatively small fraction of the Galactic plane.

Allowing for a difference in temperature of ±5 K, a distance uncertainty of ∼10%, the uncertainty on the flux calibration (15%; Schuller et al. 2009) and the fact that the dust to gas ratio and κ_ν are poorly constrained we estimate the uncertainties for the mass and column density are likely to be a factor of a few. However, these uncertainties are unlikely to have a significant impact on the overall distribution or the statistical analysis of these parameters as they are systematic and affect all structures equally.

In the upper and lower panels of Fig. 18 we plot the distribution of mass-to-length ratio of the filaments and this ratio as a function of distance. The majority of the filaments have mass-to-length ratios of M/L ∼ 200–2000 $M_\odot$ pc^{-1} and is relatively independent of distance.

5. Discussion

5.1. Filamentary structures in the Galaxy

The masses and lengths of the filaments detected in this work range from a few hundred to ∼10^4 $M_\odot$ and from ∼2–20 pc, respectively. The sizes and masses are similar to the sizes and masses of many filaments reported in the literature (e.g. IRDC 18223 – Tackenberg et al. 2014; G351 – Leurini et al. 2011, both of which appear in our catalogue). However, there have also been a number of much larger and more massive filamentary structures recently reported in the literature; these can be several hundreds of parsecs in length and have masses ∼10^5 $M_\odot$ (Ragan et al. 2014; Jackson et al. 2010; Battersby et al. 2014; Li et al. 2013; Wang et al. 2014). Many of these have been initially found from visual inspection of mid-infrared images with the aim of identifying coherent filamentary patterns

Table 4. Statistical properties of the filaments.

Parameter	Number	Mean	Standard error	Standard deviation	Median	Min	Max
Distance (kpc)	173	4.73	0.20	2.67	3.72	1.00	12.95
Length (pc)	241	5.72	0.29	4.44	4.49	1.01	35.22
FWHM width (pc)	241	0.66	0.03	0.39	0.54	0.13	2.51
Mass ($M_\odot$)	241	6137.93	685.31	10 638.86	2736.38	62.52	116 603.13
Log[Peak H_2 column density (cm^{-2})]	517	21.79	0.01	0.22	21.77	21.30	22.56
Log[Mean H_2 column density (cm^{-2})]	517	21.57	0.01	0.15	21.57	21.24	22.22
Log[RMS integrated luminosity ($L_\odot$)]	89	4.53	3.76	4.74	4.15	3.04	5.46
M/L All filaments ($M_\odot\,pc^{-1}$)	241	851.85	51.50	799.47	611.27	36.72	4761.01
M/L MSF filaments ($M_\odot\,pc^{-1}$)	72	1424.13	108.67	922.11	1288.36	214.59	4761.01

Table 5. Properties of giant molecular filaments.

Literature name	ℓ (°)	b (°)	V_{LSR} ($km\,s^{-1}$)	Distance (kpc)	Length (pc)	Log(Total Mass) ($M_\odot$)	Associations	Arm	References
GMF 18.0−16.8★	17.3	0.6	23.0	2.2	88	5.18	M16, W37	Sag.	1
GMF 20.0−17.9★	18.9	−3.3	43.5	3.4	170	5.60	W39	Scu.	1
GMF 26.7−25.4	26.0	1.4	46.0	3.1	123	5.30	···	Scu.	1
GMF 38.1−32.4a★	35.2	0.1	55.0	3.5	234	5.85	W44	···	1
GMF 38.1−32.4b★	35.1	−0.4	44.5	2.9	79	4.89	···	···	1
GMF 41.0−41.3	41.1	−0.0	38.0	2.7	51	4.69	···	···	1
GMF 54.0−52.0★	53.4	0.0	23.0	2.0	68	4.83	W52	···	1
Nessie★	338.4	−0.5	−38.0	3.1	81	5.00	···	Scu.	2
Nessie Extended★	338.3	−0.5	−40.0	3.1	162	5.30	···	Scu.	3
G32.02+0.06★	31.8	0.1	96.0	5.6	80	5.30	···	···	1, 4
G11.11−0.12★	11.2	−0.1	30.0	3.6	28	···	The Snake	···	5
Molecular Wisp	51.0	0.7	6.2	9.8	500	5.00	G52L nebula	Per.	6
CFG024.00+0.48★	24.00	0.48	96.0	5.2	82	4.9	···		7
CFG028.68−0.28	28.68	−0.28	88.2	4.89	60	4.7	···	Scu.	7
CFG029.18−0.34	29.18	0.34	93.8	3.5	99	4.7	···	Scu.	7
CFG047.06+0.26★	47.06	0.26	57.5	4.44	73	4.2	···	Sag.	7
CFG049.21−0.34★	49.21	−0.34	68.5	5.41	85	4.9	W51	Sag.	7
BC 029.94-0.30	26.94	−0.30	58	4.6	13	3.23	...	Scu.	8
BC 025.24-0.45★	25.24	−0.45	57.3	4.3	57	3.99	N40	Scu.	8
BC 018.88-0.09	18.88	−0.09	46	3.7	45	3.90	...	Scu.	8
BC 004.14-0.02	04.14	−0.02	8	3.1	37	4.04	...	Scu.	8
BC 335.31-0.29	335.31	−0.29	−42	3.2	34	4.00	...	Scu.	8
BC 332.21-0.04	332.21	−0.04	−49	3.3	52	4.20	...	Scu.	8

Notes. This table combines many of the parameters given in Tables 2 and 3 presented by Ragan et al. (2014) and includes a few similar structures reported in the literature. We identify structures that are coincident with filaments reported in this paper by appending a ★ to the literature name in Col. 1. The prefix of CF on the source name of the Wang et al. (2015) sample of filaments corresponds to *cold filament*. We have omitted the following four filaments that appear in the sample presented by Wang et al. (2015): CFG026.38+0.79 is the dense part of the larger structure GMF 26.7−25.4 identified by Ragan et al. (2014) and is therefore not considered to be an independent entity; CFG064.27−0.42 is located outside the region of interest for this study; CFG011.11−0.12 and CFG338.47−0.43 are part of the Snake and Nessie filament for which more detailed studies are available.

References. (1) Ragan et al. (2014); (2) Jackson et al. (2010); (3) Goodman et al. (2014); (4) Battersby et al. (2014); (5) Wang et al. (2014); (6) Li et al. (2013); (7) Wang et al. (2015); (8) Zucker et al. (2015).

or using the ^{13}CO (1–0) GRS data. How are these structures of different sizes related?

To address this question we have compiled a list of some of the largest structures reported in the literature. The names, positions and physical properties for these structures are given in Table 5. This sample includes 7 large filaments identified by Ragan et al. (2014) with lengths from ∼50 to 250 pc and 5 filaments identified more recently by Wang et al. (2015). To this sample we also add some of the most well-known filaments: G11.11−0.12 (the "Snake"; Wang et al. 2014), "Nessie" (Jackson et al. 2010) and G32.02+0.06 (Battersby et al. 2014) all of which have sizes of ∼100 pc. We also include the truly giant filamentary structure identified by Li et al. (2013); this has a length of ∼500 pc and consists of two connected molecular clouds (G052.42+0.74 and G051.69+0.074) that are located on the periphery of the G52L nebula (Bania et al. 2012).

Ragan et al. (2014) refers to these structures as *giant molecular filaments* (GMF) and we will adopt this terminology for structures with lengths of ∼50–200 pc. The largest filament has been identified by Li et al. (2013). These authors refer to it as a *molecular wisp*. Since only a few studies of this kind of structures have been conducted (Ragan et al. 2014; Wang et al. 2015), which are limited to relatively nearby structures locate in the northern Galactic plane, this sample of GMFs is unlikely to be complete and we have not attempted to compile an exhaustive list from the literature. However, this sample does contain some of the most well-known filaments and is representative enough

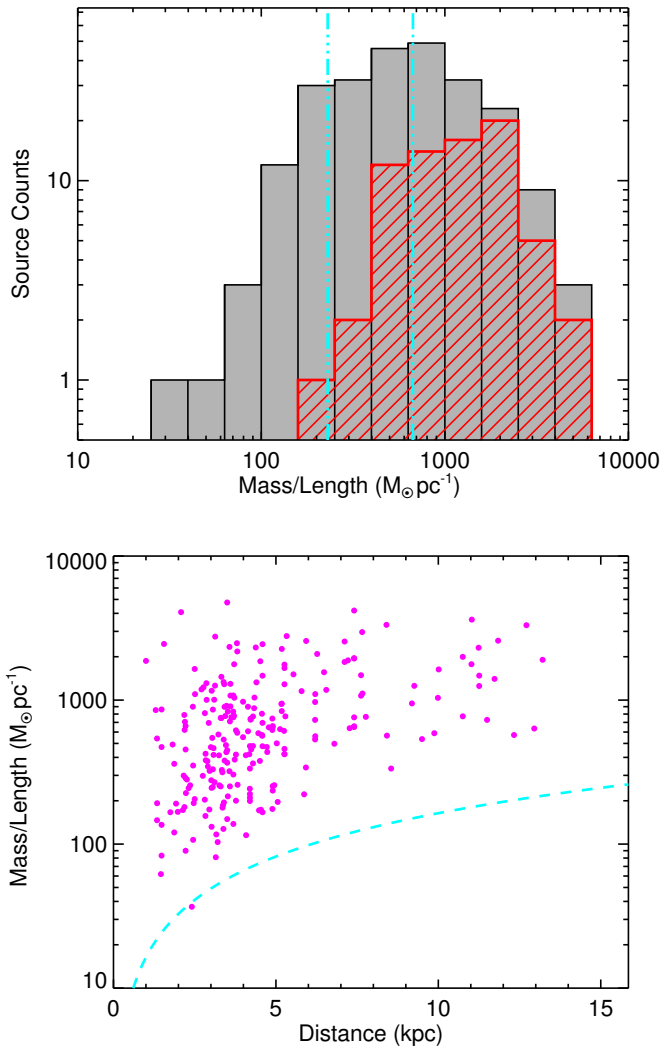

Fig. 18. *Upper panel*: mass-to-length (M/L) ratio for all filaments and for those associated with massive star forming clumps are shown as grey and red hatched histograms, respectively. The vertical cyan lines show the critical M/L thresholds for filaments with line-widths of 0.7 and 1.2 km s^{-1}; this corresponds to masses per unit length of 230 and 670 $M_\odot$ pc^{-1}, respectively. Filaments above these thresholds are unstable to radial collapse (see Sect. 5.5 for details). The bin size is 0.2 dex. *Lower panel*: the mass-to-length ratio is plotted as a function of heliocentric distance; the dashed cyan curve in this plot indicates the sensitivity of the ATLASGAL survey.

to investigate the connection between structures of different size-scales and allow their properties to be compared.

In Fig. 19 we present a size-mass diagram showing the distributions of the filaments identified here and the compilation of larger structures presented in Table 5. The GMF identified by Ragan et al. (2014) and Wang et al. (2015) are clearly much larger and more massive than the filaments presented here. However, the dense gas fractions of these structures is relatively low (e.g. 2–12% – Ragan et al. 2014) so it may be that we are tracing the dense fragments or sub-regions of these much larger structures. Comparing the positions of our sample of filaments with the GMFs we are able to find matches for 11 of the GMFs, and in a few of these cases we find multiple filaments matched to a single GMF (e.g. G016.763+00.020, G016.891+00.706, G016.919+00.268, G017.190+00.798 are associated with GMF 20.0−17.9 identified by Ragan et al. 2014).

We do not find a match for four of the GMFs: GMF 41.0–41.3, GMF 26.7−25.4, CFG028.68−0.28 and CFG029.18−0.34. However, we note that GMF 41.0−41.3 has the lowest dense gas fraction and has a total dense gas mass almost an order of magnitude lower than any of the other GMFs. We also note that approximately 50% of GMF 26.7−25.4 extends out of the region covered by ATLASGAL ($0.5° < b < 2.2°$). Furthermore, inspection of the images presented by Wang et al. (2015, their Fig. 2) reveals that CFG029.18−0.34 appears to be quite diffuse and CFG028.68−0.28 is located in a region of extended background emission and is not so easily identified (see a combined *Planck*-ATLASGAL map of this region in Csengeri et al. 2016b). We also do not find a counterpart of the molecular wisp identified by Li et al. (2013), however, in spite of its size this structure has a similar total mass as those identified by Ragan et al. (2014) and is likely to have a significantly lower column density; this source is significantly offset from the other GMF shown in Fig. 19.

In Fig. 19 we also include 6 more large filaments identified by Zucker et al. (2015). This work follows from a study by Goodman et al. (2014) where they effectively doubled the size of the Nessie filament and speculate that this structure may constitute one of many potential *bones* of the Galaxy. Among the 6 new objects, one is too close to the Galactic centre region – a region that we did not study because of the complexity of the emission. We compared positions and velocities of the remaining five objects and found that BC 025.24-0.45 is matched to our filament G025.342-0.382. We have inspected the ATLASGAL images of these new objects, and found that two of the objects (BC 026.94-0.30, BC 018.88-0.09) appear as chains of disconnected clumps, and are not identified as filaments by `DisPerSE`. This might because these objects are extremely thin, and thus are not well resolved by ATLASGAL. The remaining two of their objects (BC 335.31-0.29 and BC 332.21-0.04) are located within crowed regions of emission. As ATLASGAL is sensitive to all emission along the line of sight, these structures are more readily identified in mid-infrared extinction.

Comparing our sample of filaments with the GMFs reported in the literature we have found a match between our sample and 11 of the 16 larger scale filamentary structures discussed in the previous paragraphs; these are identified by a star appended to the literature name given to the various structures in Table 5. This supports the hypothesis that what we have detected is the dense fragments of much larger filamentary structures, and although the matched sample is relatively modest, it opens up the possibility that many more of our filaments may also be dense fragments of much larger structures. The distributions of our filaments and the GMFs shown in Fig. 19 is consistent with this possibility. A similar conclusion was reached by Schisano et al. (2014) from a comparison of the structures identified in *Herschel* maps. Relatively few large-scale structures have been identified to date but this is likely to increase in the future with the completion of a number of molecular line surveys (e.g. The Mopra Southern Galactic Plane Survey (Burton et al. 2013) and the *James Clerk Maxwell* Telescopes CO Heterodyne Inner Milky Way Plane Survey (CHIMPS; Rigby et al. 2016) at which point this hypothesis can be more robustly tested).

5.2. Orientation with respect to the Galactic mid-plane

In Sect. 3.4 we found that the filaments are preferentially aligned parallel with the Galactic mid-plane. This suggests there is a connection between the dynamics of the Galactic disk and the

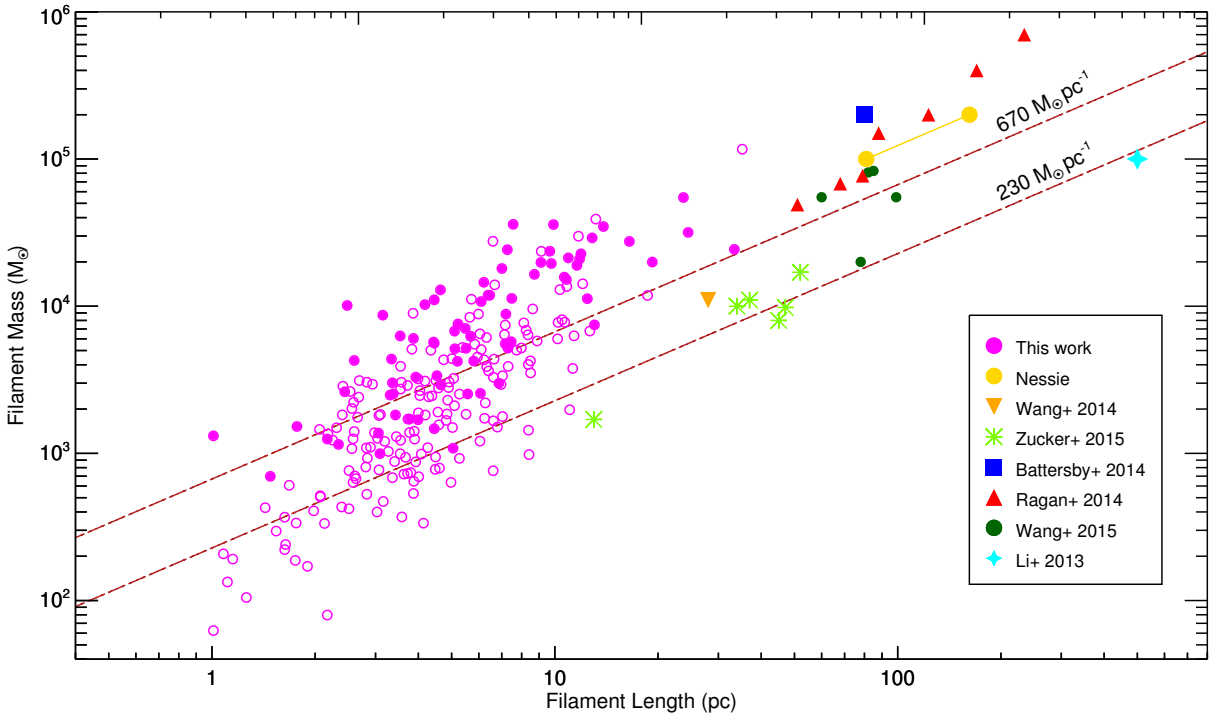

Fig. 19. Size-mass diagram of the filamentary structures discussed in Sect. 5.1. The values are taken from the original publications. This diagram illustrates the differences discussed in the text between the filaments detected in this work and giant filamentary structures reported in the literature. The "Nessie" filament is represented by two connected circles; the left circle corresponds to the structure identified by Jackson et al. (2010) while the right circle corresponds to the large structure identified by Goodman et al. (2014). The solid magenta circles identify filaments associated with massive star forming tracers while the open circles identify the non-MSF filaments. The red dashed lines correspond to the critical mass per unit length above which the filament becomes unstable and will start to collapse along their radial axis (André et al. 2014); the upper and lower line corresponds to velocity dispersions of 1.2 and 0.7 km s^{-1}, respectively, and assume an isothermal temperature of 10 K.

structure of the molecular material found within it. This connection is found both at larger scale, with the recent discovery of ≥100 pc molecular structures (Li et al. 2013; Ragan et al. 2014; Goodman et al. 2014), and small clumps (Urquhart et al. 2015) all of which are found to have their major axis preferentially aligned parallel to the Galactic mid-plane. This preferred orientation therefore seems to apply to size scales from sub-parsec to ≥100 pc and therefore extends over two orders of magnitude. A similar phenomenon can be seen in optical images of nearby face-on spiral galaxies such as M 31 and M 51 (Schinnerer et al. 2013), where filamentary dust lanes are roughly parallel to the spiral arms. The alignment between cold gas condensations and spiral arms is also nicely reproduced in simulations (Dobbs & Pringle 2013; Smith et al. 2014a). Following the discussion presented in the previous subsection it seems likely that the filaments we have identified are the high-density regions of these larger scale structures.

There are a number of explanations for the observed preferential alignment of these elongated structures with the Galactic mid-plane. These include magnetic fields and Galactic shear. Li et al. (2014) present evidence that the B-field in clouds is also aligned with the local large-scale B-field in the diffuse ISM and that the latter is further aligned with the Galactic plane (Han & Wielebinski 2002; Jansson & Farrar 2012).

This alignment is similar to what we see in our filaments. Furthermore, when these results are combined with recent observation of the alignment of the B-field in the diffuse ISM and the Galactic plane (Li et al. 2015) it suggests a picture where large-scale Galactic magnetic fields influence the dynamics of molecular gas over a wide range of scales. This is consistent with high resolution observations of the CO (2–1) emission towards six of the most massive clouds in M31 reported by Li & Henning (2011). Results from the Planck satellite (Planck Collaboration XXXV 2016) also suggest that on large scales, filamentary structures tend to align with the magnetic field[6]. In general, the mean magnetic field is both well defined and is highly correlated with the spiral arms. Although it is clear that filamentary structures are preferentially orientated parallel to the Galactic mid-plane and with the large-scale magnetic field, it is unclear if *dynamically speaking*, the magnetic field plays a role in filament formation and evolution, or that they share a common cause.

The discovery of filamentary structures that are larger than the thickness of the molecular disk (Li et al. 2013; Goodman et al. 2014; Ragan et al. 2014) provides some support for Galactic shear playing an important role in the formation of these large-scale structures. The importance of Galactic shear in star formation has been largely overlooked, probably due to the difficulty in observing structures that are larger than the cloud scale (Li et al. 2013). However, it is much easier to study the impact of shear on cloud structures in other galaxies such as M 51 (Schinnerer et al. 2013). Indeed, recent results indicate that shear does have significant impacts on cloud dynamics and

[6] In Planck Collaboration XXXV (2016), the orientation of structures is defined from the *local* density gradient. In this work, we are concerned with the *global* orientation of the structures. The density threshold of $\log 10(N_{\rm H}/{\rm cm}^{-2}) \approx 21.7$ does not contradict our results.

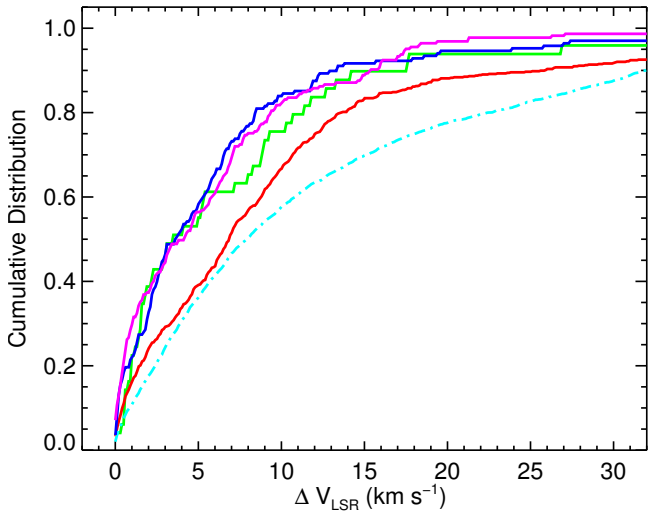

Fig. 20. Cumulative distribution of separation in velocity of filaments and molecular clouds and their nearest spiral arm long the line of sight ($|\Delta V|$). The spiral arm velocities are those shown in Fig. 11. The $|\Delta V|$ distribution of the filaments is shown by the magenta curve, which is compared to H II regions shown in blue, the 50 most massive GRS clouds shown in green and the rest of the GRS lower mass cloud population, which is shown in red. The cyan curve traces the $|\Delta V|$ distribution determined from a Monte Carlo simulated sample of clouds with random velocities.

it can disrupt the cloud and suppress star formation (Meidt et al. 2015; Colombo et al. 2014). This agrees with earlier theoretical studies (Kim & Ostriker 2006, 2002; Elmegreen & Elmegreen 1986) as well as observational arguments (Seigar 2005; Weidner et al. 2010). Although it is rather speculative at this stage, it does seem plausible that the alignment between the filaments and the Galactic disk may be the result of shear.

5.3. Correlation of filaments with the spiral arms

Figure 11 reveals a tight correlation between the spiral arms and the filaments. To quantify this correlation we follow the analysis presented by Stark & Lee (2006) and estimate the absolute difference between the radial velocity of the source and the velocity of the nearest spiral arm along its line of sight; they refer to this as the "concentration statistic" $|\Delta v|$. We use the velocities of the same spiral arms presented in Fig. 11 to determine this statistic for the filaments and compare their distribution with a number of other samples. For all of the samples considered we exclude the regions within 10° of the Galactic Centre (i.e. $350° < \ell < 10°$) as the velocities of the spiral arms are not well constrained in this region.

In Fig. 20 we present the result of this analysis in the form of a cumulative distribution of the velocity differences. In this plot we also show the results of the same analysis performed using the sample of compact H II regions identified by Urquhart et al. (2013b) from the CORNISH survey, the GRS molecular cloud catalogue (Roman-Duval et al. 2009) and a sample with a random set of velocities produced by a Monte Carlo simulation; these were produced following the method outlined in Sect. 4 of Stark & Lee (2006). For the GRS clouds we plot the 50 most massive clouds separately from the rest of the sample.

Observations of nearby spiral galaxies have revealed that young H II regions are amongst the most reliable tracers of their spiral structures (e.g. Schinnerer et al. 2013). The velocity differences between the CORNISH sample of compact H II regions and the spiral arms should therefore provide a good reference point for comparison. It is clear from Fig. 20 that the distributions of the filaments (magenta) and the H II regions (blue) are in excellent agreement with each other (p-value in a KS test is 0.11) and with the distribution of the 50 most massive GRS clouds (green; p-value is 0.14). All three samples are very tightly correlated with the spiral arms with over 80% having offsets $<10\,\mathrm{km\,s^{-1}}$. They are all significantly different from the distribution of lower mass clouds in the GRS sample (Kolmogorov-Smirnov test p-value $<1.8\times10^{-4}$ for all samples), which is likely to include a number of inter-arm clouds (~10%; Stark & Lee 2006). The difference in the distribution of the most massive clouds and the rest of the population is in excellent agreement with the findings of Stark & Lee (2006). This is in spite of the fact that we have used a different catalogue of molecular clouds and spiral arm loci, although the spiral arm loci derived by different models are in broad agreement. We note however, despite the differences in the distributions of the filaments, H II regions, massive and less massive clumps we find them all to be significantly more tightly correlated with the spiral arms than that of the randomly sampled clouds produced by the Monte Carlo simulation (cyan; with all p-values $<2\times10^{-10}$) showing the correlations are real and could not be produced by chance.

We note that Ragan et al. (2014) reported that most of their GMFs were located in the inter-arm regions; this led them to speculate that they may be analogs to the spurs observed in nearby spiral galaxies. We find that many of the filaments we have identified, which includes many identified by Ragan et al. (2014), appear to be tightly correlated with the spiral arm loci (see Figs. 11 and 20). However, we note that along many lines of sight towards the inner Galaxy the spiral arms overlap in velocity and this is likely to lead to blending of different physical structures. This makes it more difficult to identify large-scale structures associated with spiral arms than in the inter-arm regions, and might explain why Ragan et al. (2014) found the GMF to be located in the inter-arm regions. This is rather speculative and requires a more detailed investigation to verify and will be explored in a subsequent paper.

5.4. Associations with other catalogues

5.4.1. IRDCs

We have cross-matched the positions of the CSC associated with filaments (as discussed in Sect. 3.5) with the IRDC catalogue produced by Peretto & Fuller (2009). We find matches between 451 CSC sources and IRDCs and these in turn are matched with 193 of our filaments; thus 43% of the filaments associated with CSC sources are also associated with IRDCs.

As mentioned in the previous subsection many of the recent searches for filaments have used IRDCs as their starting point to identify suitable candidates whose nature as coherent filaments was later confirmed using molecular line data. These samples are therefore somewhat biased to relatively nearby structures that may not be representative of the general population. Our method of starting with the dust continuum maps has successfully recovered the majority of the filaments that were already known, many of which were discussed in the previous subsection, and has identified ~200 similar filaments that are associated with IRDCs. We have also identified a large number of structures that are not seen in extinction against a strong mid-infrared background emission and so are unlikely to have been detected by the other studies. Our sample therefore offers a more global view of their Galactic distribution and physical properties.

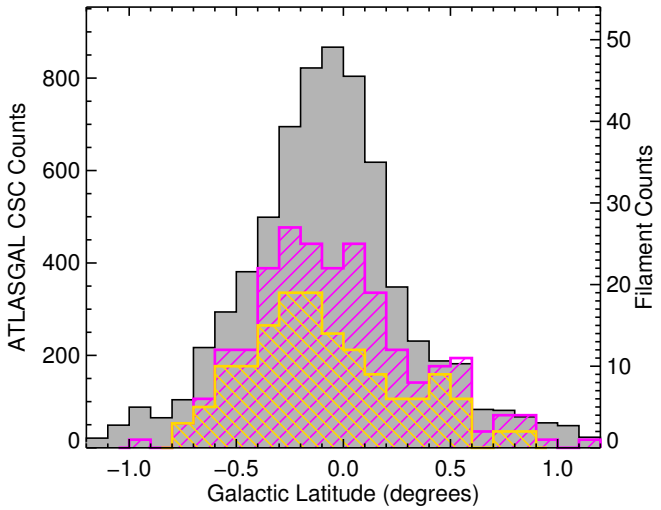

Fig. 21. Comparison of the Galactic latitude distribution of filament (magenta hatching) with respect to that of the ATLASGAL CSC (grey; $10° < |\ell| < 60°$). Filaments associated with IRDCs are shown by the yellow hatching (see text for more details). The bin size used is 0.1°.

In Fig. 21 we present the numbers of sources of the whole ATLASGAL CSC, the filaments and the filaments associated with IRDCs in grey, magenta and yellow, respectively. Since the IRDC catalogue excludes the innermost part of the Galactic plane (i.e. $350° < |\ell| < 10°$) this region has been exclude from this analysis. The filaments have a flatter distribution compared to the ATLASGAL sources and those associated with IRDCs are flatter still. Both the filaments and IRDCs appear to peak at more negative latitudes and this is probably just reflecting that these samples consist of a larger proportion of nearby structures and have a broader distribution. This gives an indication of how far out in distance we are probing with the IRDC associated being the most nearby structures while the whole sample of filaments, which is not affected by extinction, is penetrating farther through the plane.

5.4.2. Mid-infrared bubbles

`DisPerSE` is designed to follow the peaks in the emission distribution of a given structure and it takes no account of the morphology of the emission. As well as identifying filamentary structures, which are generally linear with larger aspect ratios (>3), it is sensitive to curved ridges of material often found around the periphery of evolved H II regions. These dense ridges are formed from material that is swept up in front of the ionisation front as the H II regions expand. Since the processes that lead to these dense ridges and the more linear filamentary structures are not necessarily the same it is useful to distinguish between them.

Churchwell et al. (2006) identified a large catalogue of bubbles by inspecting mid-infrared images from the GLIMPSE survey (Benjamin et al. 2003; Churchwell et al. 2009). This catalogue contains details for 322 partial and closed ring bubbles. We have searched for matches between these bubbles and the filaments using a search radius twice the size of the mean bubble radius. This has resulted in the identification of 47 filaments that are associated with bubbles, with 6 filaments associated with two bubbles. We include the names of the bubbles where a match has been found in Table 3.

In many cases the association of these filaments with bubbles is far from clear. In Fig. 22 we show some examples of these matches, which have been selected to illustrate some of the variety but also the ambiguities. In some cases the filament is indeed tracing the dense material around the edge of the H II regions as one would expect (upper panel), however, in others the filament appears to run through the middle of the bubbles (upper middle panel), while in others the filaments appear to thread their way around two bubbles (lower middle panel). Interestingly we find four bubbles that are associated with 2 or more filaments; these are bubbles N2, N18, N59 and N63. These are some of the largest bubbles identified in the Churchwell catalogue with angular radii between 6.7 and 12 arcmin – the average radius of the catalogue is ∼2′. It is therefore likely that in these cases the filaments are tracing density enhanced fragments of the molecular shell surrounding the H II regions (e.g. see lower panel of Fig. 22). It is not surprising to find many filaments on the periphery of H II regions as bubbles and shells have been found to be preferential sites of filament formation (Inutsuka et al. 2015).

5.5. Filaments as engines of star formation

In total, filaments and networks of filaments contribute ∼65% of the total flux contained in the detected structures. Assuming the temperature and distance distributions are similar for different types of structures, it is likely that they are associated with a proportional fraction of the dense gas mass (see Sect. 3.4). We found in Sect. 3.5 that the proportion of massive star forming clumps associated with the filaments is similar to their dense gas fraction. We also found that the filamentary structures (both networks and single filaments) are also associated with approximately an equal proportion of the Galactic population of MSF clumps (∼67%), suggesting a direct link between dense mass fraction and massive star formation.

In Sect. 3.5 we found that 157 MSF clumps are associated with 103 filaments, which is only 22% of the filament sample. As shown in Figs. 16 and 19 the filaments associated with MSF clumps tend to be the more massive, but have a similar range of filament lengths. For an isothermal cylinder the balance between self-gravity and the internal pressure gives a critical mass per unit length

$$M_{\rm line,crit} = \frac{2\sigma_v^2}{G} = 465 \left(\frac{\sigma_v}{1\,{\rm km\,s^{-1}}}\right)^2 M_\odot\,{\rm pc^{-1}}, \quad (7)$$

where $M_{\rm line,crit}$ is the critical virial mass per unit length and σ_v is the velocity dispersion of the gas. A detailed analysis of the stability can be found in Fiege & Pudritz (2000). Filaments with M/L ratios larger than the critical value are unstable and will collapse radially. Ammonia observations of the (1, 1) and (2, 2) inversion transitions of a large number of quiescent and massive star forming clumps reported line-widths ranging from 0.7–1.2 km s^{-1}, with the larger values found towards MYSOs and H II regions (Wienen et al. 2012; Urquhart et al. 2011; Dunham et al. 2011a). These observations were targeted at the peak column density regions and have an angular resolution ∼30–40″, which is comparable with the widths of filaments and should provide a reasonable estimate of their radial stability. Putting these values into Eq. (7) we estimate an upper and lower threshold for the critical masses of 670 and 230 $M_\odot$ pc^{-1}, respectively; these thresholds are indicated on Fig. 19 by the dashed diagonal lines.

Comparing all of the filaments discussed in Sect. 5.1 we find that nearly all of the large-scale filaments are likely to be unstable to radial collapse and fragmentation. We also find that approximately half of the filaments we have identified are likely

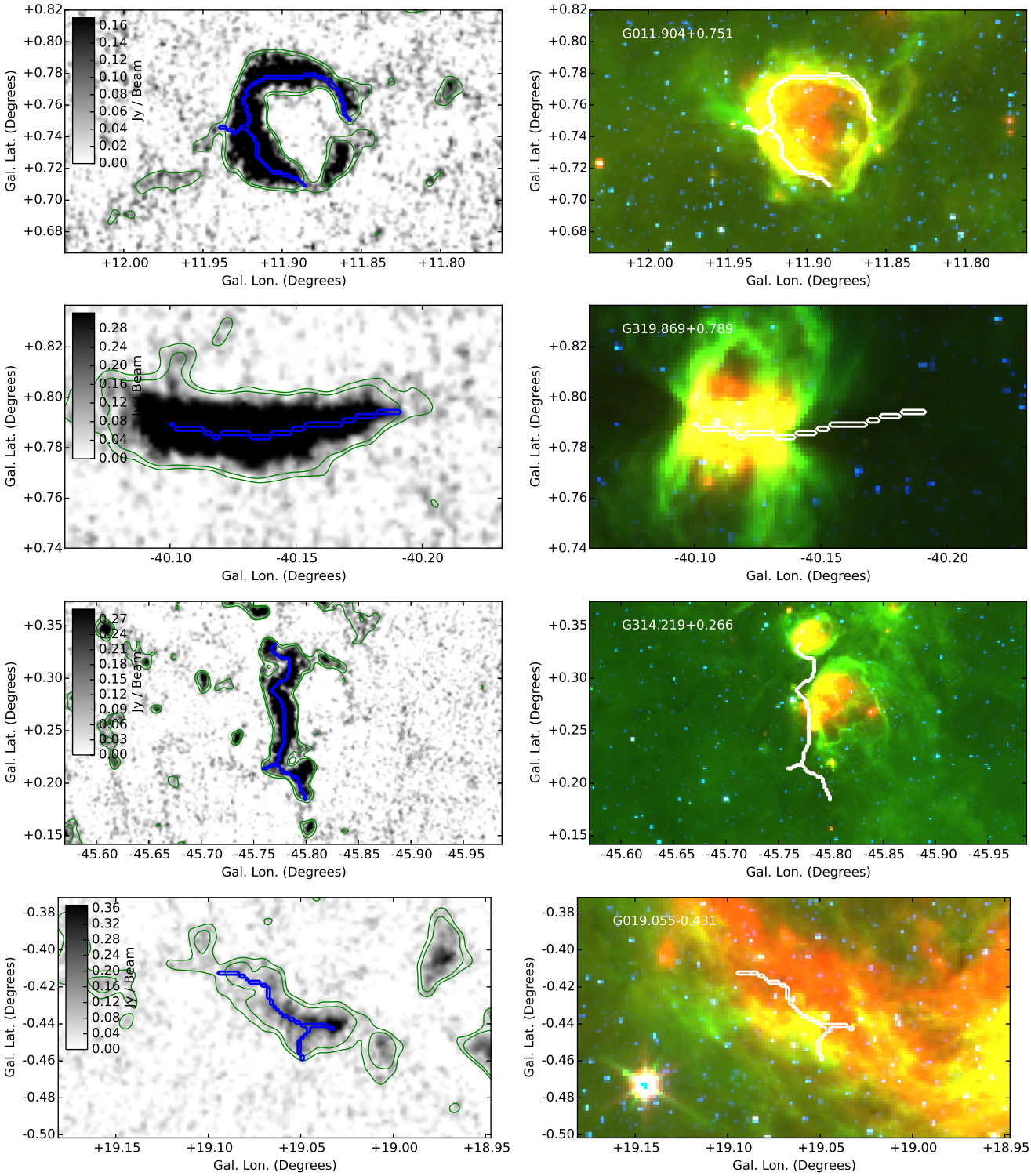

Fig. 22. Examples of filaments that correlate with GLIMPSE bubbles. In the *upper panel* we show an example of the filament tracing the dense material around the periphery of the H II region; *upper middle* shows the filament running through the centre of a bubble; *lower middle* panel shows a filament weaving round two bubbles; *lower panel* shows a filament that is tracing a section of a much more extended bubble. For image details see caption of Fig. 4.

to be unstable. We note, however, that most of the filaments associated with the MSF clumps are located above this threshold and likely to be radially collapsing. In Fig. 18 we show the M/L ratio distribution for all of the filaments as well as those associated with MSF clumps. The MSF associated filaments clearly have significantly larger M/L ratios compared to the rest of the population (KS test results in a p-value $\ll$0.0013).

There is strong correlation between filaments with the largest M/L ratio and the presence of massive star formation, and this appears to be fairly consistent with the theoretically determined critical values. This also provides a rather straightforward explanation as to why the proportion of massive star forming filaments is relatively modest (~22%). Furthermore, this analysis supports a fairly simple evolutionary sequence starting with large-scale

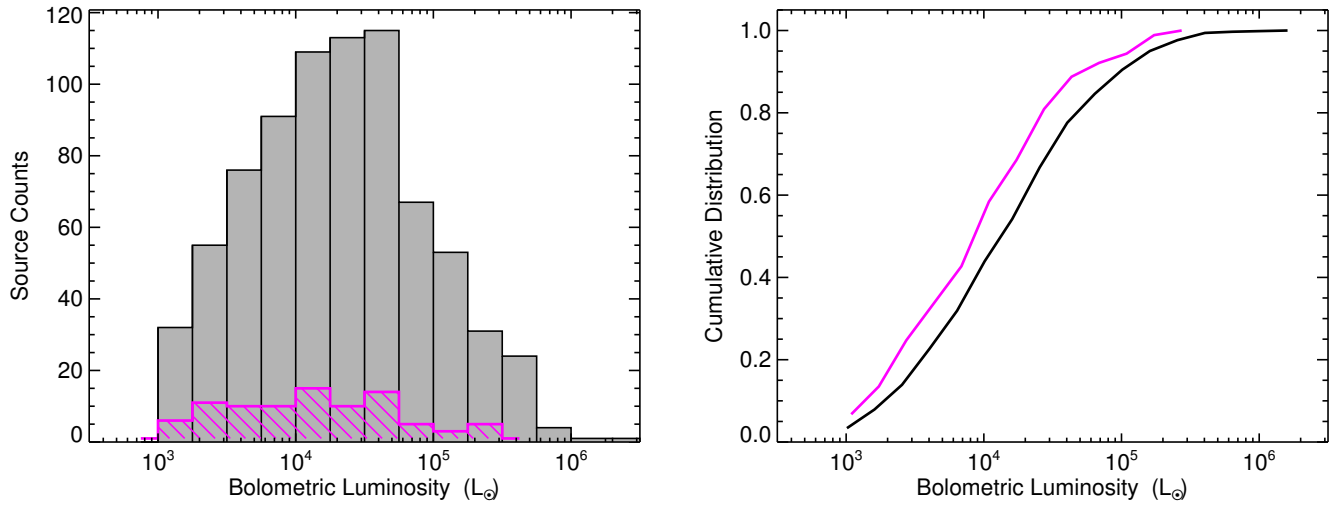

Fig. 23. Luminosity distribution of H II regions and MYSOs associated with the filaments. The *left hand panel* shows the distribution of all H II regions and MYSOs in the ATLASGAL region identified by the RMS survey (grey histogram) and those associated with a filament (magenta hatched histogram). The *right hand panel* shows the cumulative distribution of the luminosity for all massive RMS sources (black curve) and those associated with the filaments identified in this paper.

unstable filaments that form in the spiral arms; these collapse radially and fragment into denser filaments and clumps, some of these remain unstable and continue to collapse resulting in massive star formation while others fall below the critical M/L threshold and are able to resist further collapse.

In Fig. 23 we compare the luminosity distribution of all MSF clumps and those associated with filaments. In the left and right panels we present a histogram and cumulative distribution of the two samples; these show that the luminosities of the MSF clumps associated with the filaments cover almost the full range of luminosities found for MYSOs and UC H II regions, but they have a flatter distribution that slightly over-samples the lower luminosity end of the distribution. However, a KS test is unable to reject the null hypothesis that the two samples are drawn from the same parent population (p-value = 0.09). This suggests that the MSF clumps associated with filaments can be considered to be representative of the general population and that detailed follow-up studies of this relatively small sample of nearby filaments have the potential to provide valuable insights into how massive star forming clumps and their large-scale molecular environments are related.

6. Summary and conclusions

In this paper we present the results of a systematic search for filamentary structures located across the inner part of the Galaxy. This has been achieved using the `DisPerSE` algorithm which has been used to find regions of coherent dust emission in the ATLASGAL survey region ($300° < \ell < 60°$ and $|b| < 1.5°$). To improve the performance of the code we first smoothed the emission maps and decreased the resolution by a factor of 2 and used this to produce a smoothed signal-to-noise map. This improves the sensitivity to the weaker extended inter-clump regions that form the links between larger structures.

This generated a provisional catalogue of structures that was subsequently inspected resulting in the identification of 517 filamentary structures. Comparing the available velocity information we find 31 structures where the velocity dispersion is greater than 10 km s^{-1}; these are considered to be due to line of sight blending of clumps and are removed from our final sample. Comparison with the literature reveals that we have recovered the majority of the filaments previously reported that are located in the ATLASGAL survey region. In total, we have obtained velocity information for 279 of the catalogued filaments and have determined distances for 241 of the catalogued filaments.

Distances and velocities have been determined for many of the ATLASGAL sources (e.g. Wienen et al. 2012, 2015; Urquhart et al. 2014a) and these can be readily assigned to the identified structures by cross matching them to identify the dense clumps previously identified in the ATLASGAL CSC. This resulted in associations of approximately four-fifths of the CSC with the remainder being associated with weaker emission that fell below the detection threshold of the ATLASGAL CSC. We also determine the fraction of massive star formation for each structure type by matching up clumps with methanol masers, massive YSOs and H II regions identified by Urquhart et al. (2014a, and references therein).

We focus on the properties of the filaments and present the most complete view yet of their Galactic distribution and investigate their association with the spiral arms. The main results are as follows:

1. We have identified a large and reliable sample of filaments located across the inner Galactic plane. This sample consists of 486 spatially and kinematically coherent filaments with a relatively even split between the I and IV Quadrants. Most previous works have focused on filaments located in the I Quadrant and so this catalogue is the ideal tool to begin to explore the IV Quadrant.
2. The filaments identified have aspect ratios of 2–10, lengths between 2 and 20 pc, widths between ~0.1–2.5 pc and masses between $\sim 10^2$–$10^5\,M_\odot$. The filaments have typical mass-to-length ratios of $M/L \sim 200$–$2000\,M_\odot\,\mathrm{pc}^{-1}$. We find our filaments are smaller than many of the large-scale structures (~100 pc) recently reported in the literature, but are larger and significantly more massive than many of the filaments identified by *Herschel* studies. Our sample therefore covers an important range of the mass-size parameter-space that is currently not well explored.
3. We find a correlation between many of the large-scale filaments and filaments identified here, with our filaments

effectively tracing the high-column density regions of the larger structures. It is therefore likely that many of the filaments in our sample are intimately associated much larger-scale structures. In other words, these structures of different sizes should not be considered distinct, but parts of larger, coherent, hierarchical structures.

4. We find the filaments studied in this work are approximately aligned parallel to the Galactic mid-plane but with a slight inclination of ∼20°. This indicated that at ∼10 pc scale probed by the filaments, the dynamics of the Galactic disk have significant impacts on the dynamics of the dense molecular gas.
5. Comparing the velocities of the filaments with the loci of the spiral arms we show that they are tightly correlated with ∼80% of the filament velocities found within 10 km s^{-1} of that of spiral arm. A similar correlation is found for compact H II regions and for the most massive molecular clouds in the GRS survey. Plotting the distribution of the filaments on a 3D map of the Milky Way we find a good correlation with the positions of the spiral arms, and the majority of the filaments are associated with the near side of the Scutum-Centaurus arm.
6. We find ∼22% of the filaments are associated with massive star forming clumps. Comparing the properties of the filaments associated with massive star formation with the rest of the filament sample we find they are significantly more massive and have higher M/L ratios. Investigating the stability of filaments we also find that the M/L ratio for massive star forming filaments are above the critical threshold and they are therefore likely to be unstable to radial collapse. The majority of the rest of the filaments appear to be close to equilibrium, and this provides a relatively simple explanation for the low proportion of filaments that are associated with massive star formation.
7. Comparing the luminosities of massive YSOs and H II regions associated with filaments with the rest of the Galactic population of these objects we find the distributions of their luminosities are similar. This would suggest that either a significant fraction of all massive stars form in filaments or that the star formation is relatively insensitive to the large-scale structure.

In this work we provide the first Galaxy-wide sample of filamentary structures[7]. We investigate their general properties and Galactic distribution. We also investigate their association with the spiral arms, large-scale filaments, IRDCs, bubbles around evolved H II regions and regions of massive star formation. This is the largest and most comprehensive catalogue of filamentary structures in the inner Galactic plane and will provide an excellent starting point for further, more detailed studies.

Acknowledgements. We thank the referee for careful readings and helpful comments to our paper. The ATLASGAL project is a collaboration between the Max-Planck-Gesellschaft, the European Southern Observatory (ESO) and the Universidad de Chile. It includes projects E-181.C-0885, E-078.F-9040(A), M-079.C-9501(A), M-081.C-9501(A) plus Chilean data. This paper made use of information from the Red MSX Source survey database at http://rms.leeds.ac.uk/cgi-bin/public/RMS_DATABASE.cgi which was constructed with support from the Science and Technology Facilities Council of the UK. This research has made use of the SIMBAD database operated at CDS, Strasbourg, France. This work was partially funded by the ERC Advanced Investigator Grant GLOSTAR (247078) and was partially carried out within the Collaborative Research Council 956, sub-project A6, funded by the Deutsche Forschungsgemeinschaft (DFG). Guang-Xing Li and T. Csengeri are supported by the Deutsche Forschungsgemeinschaft (DFG) priority program 1573 ISM-SPP.

[7] The full catalogue and the corresponding data files are available at http://atlasgal.mpifr-bonn.mpg.de/cgi-bin/ATLASGAL_FILAMENTS.cgi

References

André, P., Men'shchikov, A., Bontemps, S., et al. 2010, A&A, 518, L102
André, P., Di Francesco, J., Ward-Thompson, D., et al. 2014, Protostars and Planets VI, 27
Arzoumanian, D., André, P., Didelon, P., et al. 2011, A&A, 529, L6
Bania, T. M., Anderson, L. D., Balser, D. S., & Rood, R. T. 2010, ApJ, 718, L106
Bania, T. M., Anderson, L. D., & Balser, D. S. 2012, ApJ, 759, 96
Battersby, C., Ginsburg, A., Bally, J., et al. 2014, ApJ, 787, 113
Battisti, A. J., & Heyer, M. H. 2014, ApJ, 780, 173
Benjamin, R. A., Churchwell, E., Babler, B. L., et al. 2003, PASP, 115, 953
Bertin, E., & Arnouts, S. 1996, A&AS, 117, 393
Brand, J., & Blitz, L. 1993, A&A, 275, 67
Bronfman, L., Nyman, L.-A., & May, J. 1996, A&AS, 115, 81
Bronfman, L., Casassus, S., May, J., & Nyman, L.-Å. 2000, A&A, 358, 521
Burkert, A., & Hartmann, L. 2004, ApJ, 616, 288
Burton, M. G., Braiding, C., Glueck, C., et al. 2013, PASA, 30, 44
Carey, S. J., Noriega-Crespo, A., Price, S. D., et al. 2005, BAAS, 37, 1252
Churchwell, E., Povich, M. S., Allen, D., et al. 2006, ApJ, 649, 759
Churchwell, E., Babler, B. L., Meade, M. R., et al. 2009, PASP, 121, 213
Colombo, D., Meidt, S. E., Schinnerer, E., et al. 2014, ApJ, 784, 4
Contreras, Y., Schuller, F., Urquhart, J. S., et al. 2013, A&A, 549, A45
Cordes, J. M. 2004, in Milky Way Surveys: The Structure and Evolution of our Galaxy, eds. D. Clemens, R. Shah, & T. Brainerd, ASP Conf. Ser., 317, 211
Csengeri, T., Urquhart, J. S., Schuller, F., et al. 2014, A&A, 565, A75
Csengeri, T., Leurini, S., Wyrowski, F., et al. 2016a, A&A, 586, A149
Csengeri, T., Weiss, A., Wyrowski, F., et al. 2016b, A&A, 585, A104
Cyganowski, C. J., Whitney, B. A., Holden, E., et al. 2008, AJ, 136, 2391
Dame, T. M., Hartmann, D., & Thaddeus, P. 2001, ApJ, 547, 792
Davies, B., Clark, J. S., Trombley, C., et al. 2012, MNRAS, 419, 1871
Dempsey, J. T., Thomas, H. S., & Currie, M. J. 2013, ApJS, 209, 8
Dobbs, C. L., & Pringle, J. E. 2013, MNRAS, 432, 653
Dunham, M. K., Robitaille, T. P., Evans, II, N. J., et al. 2011a, ApJ, 731, 90
Dunham, M. K., Rosolowsky, E., Evans, II, N. J., Cyganowski, C., & Urquhart, J. S. 2011b, ApJ, 741, 110
Ellsworth-Bowers, T. P., Glenn, J., Rosolowsky, E., et al. 2013, ApJ, 770, 39
Ellsworth-Bowers, T. P., Rosolowsky, E., Glenn, J., et al. 2015, ApJ, 799, 29
Elmegreen, B. G., & Elmegreen, D. M. 1986, ApJ, 311, 554
Federrath, C. 2016, MNRAS, 457, 375
Fiege, J. D., & Pudritz, R. E. 2000, MNRAS, 311, 85
Giannetti, A., Wyrowski, F., Brand, J., et al. 2014, A&A, 570, A65
Goldsmith, P. F., Heyer, M., Narayanan, G., et al. 2008, ApJ, 680, 428
Gómez, G. C., & Vázquez-Semadeni, E. 2014, ApJ, 791, 124
Goodman, A. A., Alves, J., Beaumont, C. N., et al. 2014, ApJ, 797, 53
Green, J. A. A. 2009, MNRAS, 392, 783
Green, J. A., & McClure-Griffiths, N. M. 2011, MNRAS, 417, 2500
Han, J.-L., & Wielebinski, R. 2002, Chin. J. Astron. Astrophys., 2, 293
Heitsch, F., Hartmann, L. W., Slyz, A. D., Devriendt, J. E. G., & Burkert, A. 2008, ApJ, 674, 316
Hennebelle, P. 2013, A&A, 556, A153
Hildebrand, R. H. 1983, Quant. J. Roy. Astron. Soc., 24, 267
Hill, T., Motte, F., Didelon, P., et al. 2011, A&A, 533, A94
Hill, T., André, P., Arzoumanian, D., et al. 2012, A&A, 548, L6
Hoare, M. G., Purcell, C. R., Churchwell, E. B., et al. 2012, PASP, 124, 939
Inutsuka, S.-i., Inoue, T., Iwasaki, K., & Hosokawa, T. 2015, A&A, 580, A49
Jackson, J. M., Bania, T. M., Simon, R., et al. 2002, ApJ, 566, L81
Jackson, J. M., Rathborne, J. M., Shah, R. Y., et al. 2006, ApJS, 163, 145
Jackson, J. M., Finn, S. C., Rathborne, J. M., Chambers, E. T., & Simon, R. 2008, ApJ, 680, 349
Jackson, J. M., Finn, S. C., Chambers, E. T., Rathborne, J. M., & Simon, R. 2010, ApJ, 719, L185
Jackson, J. M., Rathborne, J. M., Foster, J. B., et al. 2013, PASA, 30, 57
Jansson, R., & Farrar, G. R. 2012, ApJ, 757, 14
Kauffmann, J., Bertoldi, F., Bourke, T. L., Evans, II, N. J., & Lee, C. W. 2008, A&A, 487, 993
Kim, W.-T., & Ostriker, E. C. 2002, ApJ, 570, 132
Kim, W.-T., & Ostriker, E. C. 2006, ApJ, 646, 213
Leurini, S., Pillai, T., Stanke, T., et al. 2011, A&A, 533, A85
Li, H.-B., & Henning, T. 2011, Nature, 479, 499
Li, G.-X., Wyrowski, F., Menten, K., & Belloche, A. 2013, A&A, 559, A34
Li, H.-B., Goodman, A., Sridharan, T. K., et al. 2014, Protostars and Planets VI, 101

Li, H.-B., Yuen, K. H., Otto, F., et al. 2015, Nature, 520, 518
Lumsden, S. L., Hoare, M. G., Urquhart, J. S., et al. 2013, ApJS, 208, 11
Meidt, S. E., Hughes, A., Dobbs, C. L., et al. 2015, ApJ, 806, 72
Men'shchikov, A. 2013, A&A, 560, A63
Men'shchikov, A., André, P., Didelon, P., et al. 2010, A&A, 518, L103
Minier, V., Ellingsen, S. P., Norris, R. P., & Booth, R. S. 2003, A&A, 403, 1095
Miville-Deschênes, M.-A., Martin, P. G., Abergel, A., et al. 2010, A&A, 518, L104
Moeckel, N., & Burkert, A. 2015, ApJ, 807, 67
Molinari, S., Swinyard, B., Bally, J., et al. 2010, PASP, 122, 314
Molinari, S., Schisano, E., Faustini, F., et al. 2011, A&A, 530, A133
Murray, N., & Rahman, M. 2010, ApJ, 709, 424
Ossenkopf, V., & Henning, T. 1994, A&A, 291, 943
Padoan, P., Juvela, M., Goodman, A. A., & Nordlund, Å. 2001, ApJ, 553, 227
Palmeirim, P., André, P., Kirk, J., et al. 2013, A&A, 550, A38
Peretto, N., & Fuller, G. A. 2009, A&A, 505, 405
Planck Collaboration XXXV. 2016, A&A, 586, A138
Press, W. H., Teukolsky, S. A., Vetterling, W. T., & Flannery, B. P. 1992, Numerical recipes in FORTRAN, The art of scientific computing
Purcell, C. R., Longmore, S. N., Walsh, A. J., et al. 2012, MNRAS, 426, 1972
Purcell, C. R., Hoare, M. G., Cotton, W. D., et al. 2013, ApJS, 205, 1
Ragan, S. E., Henning, T., Tackenberg, J., et al. 2014, A&A, 568, A73
Reid, M. J., Menten, K. M., Brunthaler, A., et al. 2014, ApJ, 783, 130
Rigby, A. J., Moore, T. J. T., Plume, R., et al. 2016, MNRAS, 456, 2885
Roman-Duval, J., Jackson, J. M., Heyer, M., et al. 2009, ApJ, 699, 1153
Schinnerer, E., Meidt, S. E., Pety, J., et al. 2013, ApJ, 779, 42
Schisano, E., Rygl, K. L. J., Molinari, S., et al. 2014, ApJ, 791, 27
Schlingman, W. M., Shirley, Y. L., Schenk, D. E., et al. 2011, ApJS, 195, 14
Schneider, S., & Elmegreen, B. G. 1979, ApJS, 41, 87
Schuller, F., Menten, K. M., Contreras, Y., et al. 2009, A&A, 504, 415
Seigar, M. S. 2005, MNRAS, 361, L20
Shirley, Y. L., Ellsworth-Bowers, T. P., Svoboda, B., et al. 2013, ApJS, 209, 2
Smith, R. J., Glover, S. C. O., Clark, P. C., Klessen, R. S., & Springel, V. 2014a, MNRAS, 441, 1628
Smith, R. J., Glover, S. C. O., & Klessen, R. S. 2014b, MNRAS, 445, 2900
Sousbie, T. 2011, MNRAS, 414, 350
Stark, A. A., & Lee, Y. 2006, ApJ, 641, L113
Tackenberg, J., Beuther, H., Henning, T., et al. 2014, A&A, 565, A101
Taylor, J. H., & Cordes, J. M. 1993, ApJ, 411, 674
Ungerechts, H., & Thaddeus, P. 1987, ApJS, 63, 645
Urquhart, J. S., Busfield, A. L., Hoare, M. G., et al. 2007, A&A, 474, 891
Urquhart, J. S., Busfield, A. L., Hoare, M. G., et al. 2008, A&A, 487, 253
Urquhart, J. S., Morgan, L. K., Figura, C. C., et al. 2011, MNRAS, 418, 1689
Urquhart, J. S., Moore, T. J. T., Schuller, F., et al. 2013a, MNRAS, 431, 1752
Urquhart, J. S., Thompson, M. A., Moore, T. J. T., et al. 2013b, MNRAS, 435, 400
Urquhart, J. S., Csengeri, T., Wyrowski, F., et al. 2014a, A&A, 568, A41
Urquhart, J. S., Figura, C. C., Moore, T. J. T., et al. 2014b, MNRAS, 437, 1791
Urquhart, J. S., Moore, T. J. T., Csengeri, T., et al. 2014c, MNRAS, 443, 1555
Urquhart, J. S., Figura, C. C., Moore, T. J. T., et al. 2015, MNRAS, 452, 4029
Vázquez-Semadeni, E., Banerjee, R., Gómez, G. C., et al. 2011, MNRAS, 414, 2511
Walsh, A. J., Burton, M. G., Hyland, A. R., & Robinson, G. 1998, MNRAS, 301, 640
Wang, K., Zhang, Q., Testi, L., et al. 2014, MNRAS, 439, 3275
Wang, K., Testi, L., Ginsburg, A., et al. 2015, MNRAS, 450, 4043
Weidner, C., Bonnell, I. A., & Zinnecker, H. 2010, ApJ, 724, 1503
Wienen, M., Wyrowski, F., Schuller, F., et al. 2012, A&A, 544, A146
Wienen, M., Wyrowski, F., Menten, K. M., et al. 2015, A&A, 579, A91
Wienen, M., et al. 2016, submitted
Williams, J. P., Blitz, L., & McKee, C. F. 2000, Protostars and Planets IV, 97
Zucker, C., Battersby, C., & Goodman, A. 2015, ApJ, 815, 23